The Astrophysical Journal, 966:189 (18pp), 2024 May 10 https://doi.org/10.3847/1538-4357/ad35c8

Automated Chemical Reaction Network Generation and Its Application to Exoplanet Atmospheres

Jeehyun Yang[1] and Renyu Hu[1,2]
[1] Jet Propulsion Laboratory, California Institute of Technology, Pasadena, CA 91109, USA; jeehyun.yang@jpl.nasa.gov, renyu.hu@jpl.nasa.gov
[2] Division of Geological and Planetary Sciences, California Institute of Technology, Pasadena, CA 91125, USA
Received 2024 January 26; revised 2024 March 6; accepted 2024 March 7; published 2024 May 7

Abstract

With the advent of JWST and the spectroscopic characterization of exoplanet atmospheres in unprecedented detail, there is a demand for more complete pictures of chemical and photochemical reactions and their impacts on atmospheric composition. Traditionally, building reaction networks for (exo)planetary atmospheres involves manually tracking relevant species and reactions, a time-consuming and error-prone process. This approach's applicability is also often limited to specific conditions, making it less versatile for different planetary types (i.e., photochemical networks for Jupiters may not be directly applicable to water-rich exoplanets). We introduce an automated approach using a computer-aided chemical reaction network generator, combined with a 1D photochemical kinetic-transport model, offering significant advantages. This approach automatically selects reaction rates through a rate-based iterative algorithm and multiple refinement steps, enhancing model reliability. Also, this approach allows for the efficient simulation of diverse chemical environments, from hydrogen to water, carbon dioxide, and nitrogen-dominated atmospheres. Using WASP-39b and WASP-80b as examples, we demonstrate our approach's effectiveness, showing good agreement with recent JWST data. Our WASP-39b model aligns with prior studies and JWST observations, capturing photochemically produced sulfur dioxide. The WASP-80b model reveals an atmosphere influenced by deep-interior thermochemistry and vertical mixing, consistent with JWST NIRCam observations. Furthermore, our model identifies a novel initial step for the N_2–NH_3–HCN pathway that enhances the efficiency of the conversion in high-temperature/high-pressure environments. This automated chemical network generation offers a novel, efficient, and precise framework for studying exoplanetary atmospheres, marking a significant advancement over traditional modeling techniques.

Unified Astronomy Thesaurus concepts: Exoplanet atmospheres (487); Exoplanet atmospheric composition (2021); Planetary atmospheres (1244); Theoretical models (2107); Astrochemistry (75)

Supporting material: tar.gz file

1. Introduction

Our knowledge of other stellar systems and their accompanying planets has been expanding significantly since the exoplanet surveys of Kepler, K2, and the Transiting Exoplanet Survey Satellite. Over 5500 exoplanets have been confirmed.[3] Adding to this, the recent launch of JWST has provided us with a deluge of high-quality spectroscopic data. This allows for the characterization of exoplanet atmospheres in unprecedented detail, as exemplified by the detection of SO_2 in the hot Jupiter WASP-39 b's atmosphere, which indicates active photochemistry (Tsai et al. 2023). Another example is the detection of CO_2 in the temperate sub-Neptune K2-18 b's atmosphere (Madhusudhan et al. 2023), which supports the hypothesis of a water-rich interior (Hu et al. 2021; Madhusudhan et al. 2021), but can also potentially be explained by a high-metallicity atmosphere (Hu et al. 2021; Tsai et al. 2021; Yu et al. 2021; Wogan et al. 2024).

As shown above, JWST enables detailed atmospheric measurements of diverse types of exoplanets from Jupiter-sized to Earth-sized, from cool to hot atmospheres, for which one may expect diverse atmospheric composition and redox conditions. 1D photochemical atmospheric modeling is crucial for interpreting the JWST observations as well as guiding future observations. Thus, enhancing 1D photochemical atmospheric modeling with more comprehensive chemical and photochemical reaction networks enables more precise characterizations of exoplanet atmospheres, guiding future observations and advancing our understanding of exoplanets.

Multiple photochemical reaction networks have already been developed for exoplanet atmospheric modeling studies (e.g., Moses et al. 2011; Hu et al. 2012; Venot et al. 2012; Tsai et al. 2017; Rimmer & Rugheimer 2019). However, there are still several limitations in constructing these chemical reaction networks applicable to exoplanet atmospheric conditions. One of the major issues is the way photochemical networks are constructed. Most of these existing chemical networks that describe various exoplanet atmospheres are constructed by hand, adopting reaction rate and thermodynamic parameters by carefully keeping track of all possible species and reactions relevant to the target system (e.g., Moses et al. 2011; Hu et al. 2012; Venot et al. 2012; Tsai et al. 2017, 2021; Rimmer & Rugheimer 2019). This process is very time-consuming and error-prone, and the resulting model significantly depends on the chemistry knowledge of the builder who manually chooses the parameters from various sources (i.e., laboratory measurements, ab initio calculations, estimations, etc.). For this reason, the possibility of missing and dubious reactions being included

[3] https://exoplanets.nasa.gov/

in the model increases as the model size grows, eventually leading to a failure in precisely predicting and interpreting important reaction species and pathways.

A recent study by Veillet et al. (2024) constructed C–H–O–N chemical networks based on an extensive amount of experimental combustion data gathered over recent decades. This provides a relatively robust chemical network for describing the atmospheres of hot Jupiter exoplanets, predominantly composed of H_2 with an insignificant amount of sulfur species (since the network does not contain sulfur-bearing species). However, the applicability of such a model to other types of planets is limited, often necessitating significant time and effort to develop another model for another system. This limitation arises because the relevance of the specific chemical species and reactions is intrinsically tied to the system's conditions, such as temperature, pressure, and the dominant gas species. As a result, the chemical network built by Veillet et al. (2024), while built with an intent to model H_2-dominated atmospheres only, is not applicable for, e.g., Venus-like exoplanet atmospheres, given the differences in temperature and pressure profiles as well as in the dominant atmospheric gas composition (e.g., a CO_2-dominated atmosphere with sulfur-bearing species). While some might suggest including all known species and reactions studied so far, doing so is impractical. The computational time required for large chemical kinetics simulations scales approximately linearly with the number of chemical reactions and approximately quadratically with the number of chemical species, N (Schwer et al. 2002). Given the vast amount of spectroscopic data expected from JWST and future observational missions, a fundamentally new approach to photochemical reaction network construction is essential.

Over the past decade, advancements in computational chemical engineering have paved the way for automated chemical reaction network generation. These automation techniques can be categorized based on their approaches to species and reaction selection as well as parameter generation. One common method is to define reaction families to find possible reactions, which allows for the expansion of the network, starting from an initial set of molecules (e.g., Sarathy et al. 2012). Another approach is a rule-based method, as adopted by packages like Genesys (e.g., Vandewiele et al. 2012). The inclusion of species and reactions in the network is determined by a set of user-defined constraints. Although computationally efficient, these constraints, often dependent on the user's chemistry knowledge, can potentially bias network generation. In contrast, the Reaction Mechanism Generator (RMG; Gao et al. 2016; Liu et al. 2021; Johnson et al. 2022) employs a rate-based method, where the importance of a species or reaction is determined based on iterative simulations of the chemical system. For this reason, this rate-based approach is more objective (i.e., independent of the user's chemistry knowledge) and can provide a more comprehensive chemical network than other methods. The only downside of this rate-based method is that it is computationally more expensive than other methods. These RMG-generated networks have been actively utilized in various chemical engineering fields, such as a computer-generated acetylene pyrolysis model by Liu et al. (2020), which successfully described the previous experiment by Norinaga et al. (2008), the butyl acetate pyrolysis and combustion model by Dong et al. (2023), and the methyl propyl ether pyrolysis and oxidation model by Johnson et al. (2021), showing excellent agreement with most of the shock tube and rapid compression machine data. Notably, this automation has recently been used to simulate and successfully rationalize the previous laboratory photochemical studies by Fleury et al. (2019, 2020) that simulated hot-Jupiter-like atmospheric conditions (Yang et al. 2023). Such applications underscore the reliability and vast potential of automated reaction network generators, particularly when used together with existing photochemical reaction networks, offering solutions to challenges associated with manual methodologies.

Given the challenges and potential of recent advancements in computational chemical engineering, we develop the atmospheric chemistry module of the ExoPlanet Atmospheric Chemistry and Radiative Interaction Simulator (EPACRIS), an innovative atmospheric simulation framework for exoplanets. The atmospheric radiative transfer module of EPARCRIS will be described in a separate paper (M. Scheucher & R. Hu 2024, in preparation). The EPACRIS atmospheric chemistry module integrates cutting-edge automated chemical reaction network generation by RMG with a general-purpose 1D photochemical kinetic-transport atmospheric simulation, originally developed by Hu et al. (2012), and since then expanded and upgraded substantially (Hu et al. 2013; Hu & Seager 2014; Hu 2019, 2021). This integration facilitates the fast and reliable construction of tailored reaction networks for specific exoplanet atmospheres. This paper details our methodology and demonstrates its effectiveness using the well-characterized atmosphere of WASP-39 b and the atmosphere of WASP-80 b as case studies for two different types of H_2-dominated hot or warm Jupiters, compared with recent JWST observations and photochemical modeling studies (Ahrer et al. 2023; Alderson et al. 2023; Bell et al. 2023; Feinstein et al. 2023; JWST Early Release Science Team et al. 2023; Rustamkulov et al. 2023; Tsai et al. 2023; Powell et al. 2024).

2. Methods

A schematic diagram of the methodology and the overall workflow adopted in this study are provided in Figure 1.

2.1. Automatic Chemical Reaction Network Generation Using the RMG Software

A detailed chemical reaction network for modeling the H_2-dominated atmospheres of warm and hot Jupiters with equilibrium temperatures of 800–1500 K (T_{eq} of WASP-39 b and WASP-80 b are within this range) was constructed automatically by RMG (Gao et al. 2016; Johnson et al. 2022). RMG is a Python-based open-source software and has been extensively used in the chemical engineering community to automatically generate chemical networks to simulate numerous examples of pyrolysis and combustion chemistry successfully (Class et al. 2016; Dana et al. 2018; Chu et al. 2019; Keceli et al. 2019; Liu et al. 2020). RMG was previously described in detail in Gao et al. (2016), Liu et al. (2021), and Johnson et al. (2022), and is only briefly described here along with Figure 1. A supplementary .tar.gz archive is available in the online journal and includes the RMG input file, CHEMKIN format file, and EPACRIS format file.

In given reactor conditions (i.e., temperature, pressure, reaction time, and the initial mixing ratio of gas species), RMG will first place the initial species in the reaction system

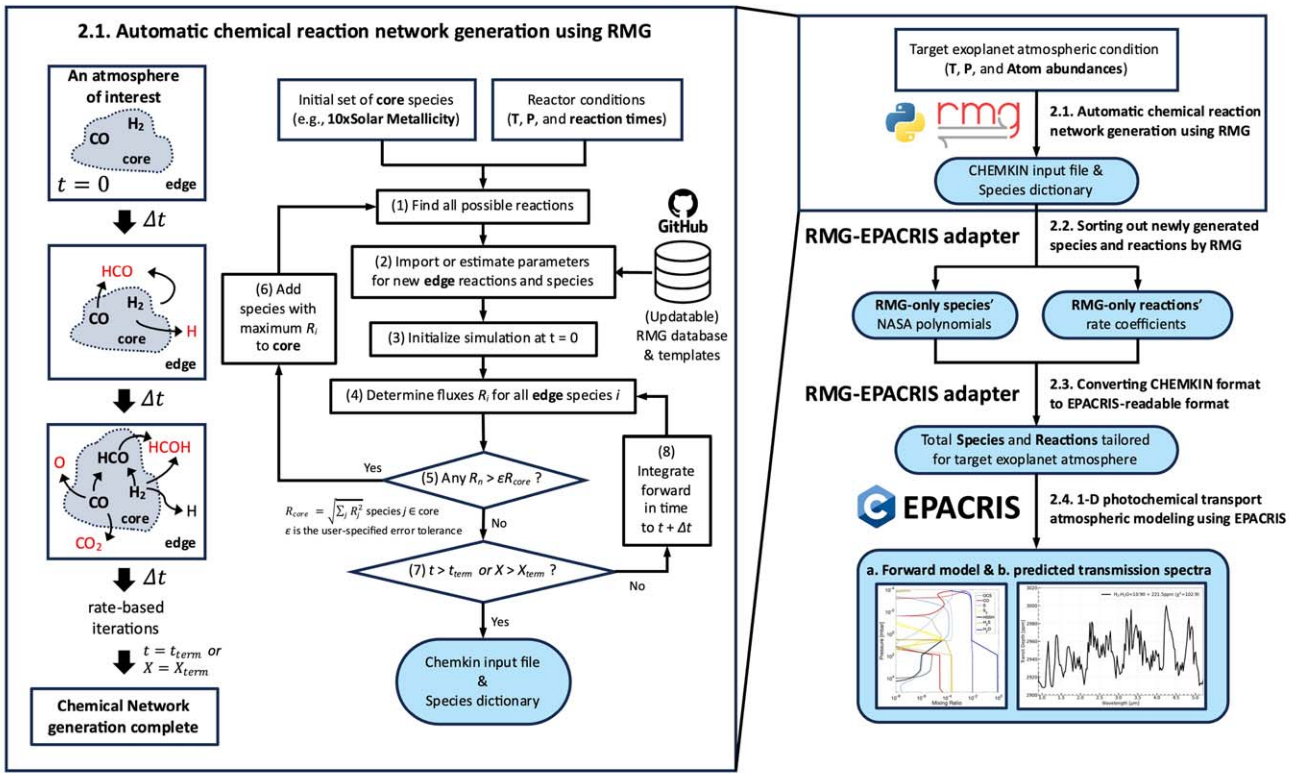

NOTE— Mention of any commercial product, process, or service by name, trademark, or manufacturer does not imply endorsement by the U.S. Government or the Jet Propulsion Laboratory, California Institute of Technology

Figure 1. A schematic diagram with a flowchart describing the expansion of the chemical network during automated reaction network generation by RMG using the rate-based algorithm (left) and the overall workflow of the implementation into 1D photochemical transport atmospheric modeling (right) in this work. RMG stands for the Python-written Reaction Mechanism Generator (Gao et al. 2016; Liu et al. 2021; Johnson et al. 2022), while EPACRIS stands for the overall ExoPlanet Atmospheric Chemistry and Radiative Interaction Simulator, written in C. Each light-blue-colored shaded box refers to the corresponding output after each method described in Section 2.

into the "core" of the model and then find all the possible reactions based on these "core" species (i.e., indicated as (1) on the left side of Figure 1). The chemical reaction rates depend on the species concentrations at the previous time step. Thus, determining this initial set of core species is crucial when applying automatic reaction mechanism generation to (exo) planetary atmospheres. Unlike laboratory experiments, where initial concentrations are well controlled, such information is often not fully available for exoplanet atmospheres. In response to this challenge, there are several ways to address this issue.

One approach to setting the initial conditions is based on existing observational constraints. For instance, the recent JWST observation of K2-18 b has constrained concentrations of certain chemical species, such as methane (CH_4) and carbon dioxide (CO_2), from atmospheric retrievals (Madhusudhan et al. 2023). Building on this, researchers can construct the chemical network of interest by assuming specific compositions—e.g., approximately 50% H_2O and 50% H_2, along with constraints on CH_4, CO_2, and $(CH_3)_2S$, which is tailored to explore the "Hycean Worlds" scenario of K2-18 b proposed by Madhusudhan et al. (2021).

Alternatively, one can define a set of grids, such as by varying solar metallicity (Lodders 2020) from $1\times$ to $100\times$solar metallicity as inputs for RMG and building a chemical network for different solar metallicities. Benchmarking these networks against existing JWST observations can check the feasibility of each chemical network. In the context of planetary atmospheres, constructing a chemical network tailored for a CO_2-dominated atmosphere with a trace amount of sulfur species can provide insights into the atmospheres of Venus or Venus-like exoplanets. Such applications offer invaluable insights into (exo)planetary atmospheres.

After the reactor condition is provided, the next step for RMG (indicated as (2) in Figure 1) is to simulate the possible reactions, using its database (maintained and updated with the latest data sources; Developers of RMG 2024) of reaction parameters from previous experiments, ab initio calculations, or estimation methods (e.g., Benson group additivity; Benson & Buss 2004), which will generate a list of possible product species (i.e., "edge" species). It should be noted that RMG relies on a chemical kinetics database compiled from various sources, each with its inherent errors. However, a well-maintained database represents our best knowledge at any given time. RMG initializes the simulation at $t = 0$ (indicated as (3) in Figure 1), followed by the next steps (indicated as (4)–(6) in Figure 1) that determine if these "edge" species are important enough to be added to the "core" species. "Edge" species i are included into the "core" species if

$$R_i = \frac{dC_i}{dt} > \epsilon R_{\rm core}, \tag{1}$$

where R_i is the production and loss flux of "edge" species i, defined as an infinitesimal change in the concentration of "edge" species (i.e., dC_i) in an infinitesimal time (i.e., dt), ϵ is the user-specified error tolerance, and R_{core} is the characteristic

flux of the reaction system, defined by

$$R_{\text{core}} = \sqrt{\sum_j R_j^2} \text{ species } j \in \text{ core.} \quad (2)$$

A typically recommended range for this user-specified error tolerance, ϵ, is between 0.01 and 0.05 for users seeking a larger and more comprehensive model, despite the higher computational cost. Consequently, ϵ is set to 0.1 in this work (as specified by `toleranceMoveToCore = 0.1` in the RMG input file, available in the supplementary .tar.gz archive). As shown in (7)–(8) in Figure 1, the reaction generation and integration steps continue until they meet the termination criteria for the reaction time, t_{term}, or the concentration of a specific species, X_{term}. This process results in the completed chemical network, encompassing all "core" species and reactions with significant fluxes at the given reactor conditions.

In this work, temperatures from 700 to 2000 K and pressures between 10^{-3} and 10^{2} bar are sampled to generate relevant chemical networks within these T and P ranges, using the ranged reactors setting in RMG (Liu et al. 2021), then later combined. We used an initial molecular mixing ratio of 10× solar metallicity, following the previous models of WASP-39 b (Tsai et al. 2023) and WASP-80 b (Bell et al. 2023), and automatically generated a chemical network. The reaction time criterion, t_{term}, was set to 3.154×10^{16} s, or 10^{9} yr, assuming the reaction time required for the reaction to achieve chemical equilibrium. The choice of the reaction libraries (`Klippenstein_Glaborg2016`, `primarySulfurLibrary`, `primaryNitrogenLibrary`, `NOx2018`, and `Nitrogen_Glaborg_Gimenez_et_al`) and thermochemical libraries (`SABIC_aromatics`, `primaryThermoLibrary`, `BurkeH2O2`, `thermo_DFT_CCSDF112_BAC`, `DFT_QCI_thermo`, `Klippenstein_Glaborg2016`, `CH`, `primaryNS`, and `SulfurGlarborgMarshall`) from which RMG retrieves the rate parameters during the chemical network generation can be found in the RMG input file (see the supplementary .tar.gz archive), and the details of these libraries (e.g., rate constants, references, etc.) can be found in the RMG database (Developers of RMG 2024). The pressure dependence feature of RMG was enabled to automatically construct pressure-dependent networks for species with up to 10 atoms (i.e., constraining a total number of atoms). The resulting chemical network contained 105 species and 2337 reactions (forward–reverse reaction pairs), which can be found in the supplementary .tar.gz archive as the CHEMKIN input file. Among these 2337 generated reactions, 2271 reactions did not violate their respective collision limits, k_{coll} (i.e., any bimolecular reaction rate coefficient does not exceed its Lennard-Jones collision rate constant), which were then incorporated into our 1D kinetic-transport model (Section 2.4) after the adaptation described in Sections 2.2 and 2.3.

2.2. Sorting Out Newly Generated Species and Reactions from RMG

Besides the RMG-generated reactions and species outlined in Section 2.1, our initial kinetic-transport atmosphere model already possesses a reaction library that includes photodissociation and associated reactions. This library comprises 111 species (see Table 1) and 914 reactions, broken down as follows: 657 bimolecular reactions, 91 termolecular reactions, 93 thermodissociation reactions, and 71 photochemistry reactions (Hu et al. 2012; Hu & Seager 2014; Hu 2021). The rates of photochemical reactions are calculated according to Equation (12) in Section 2.3 of Hu et al. (2012). Because RMG does not generate photochemistry-driven reactions, it is necessary to combine the original reaction network and the network generated by RMG, and the first step is to identify any overlapping species and reactions to prevent duplicates. We have annotated the 111 original species using RMG's "adjacency lists" methodology (Gao et al. 2016; Johnson et al. 2022), which allows the RMG-EPACRIS adapter to compare the reactants and products, including reverse reactions, and ensure no duplications. The adjacency lists method uses a graph-based structure to illustrate molecules, identifying atoms as vertices and their connecting bonds as edges in the list. For example, the adjacency lists for hydroxymethylene (HCOH) and methoxy radical (CH_3O) are shown in Figure 2.

The structure of the adjacency lists method is defined as follows. The first column specifies the atom index, the second column specifies the atom element, and the third column—prefixed by the lowercase letter "u" for "unpaired"—specifies the count of unpaired electrons for each atom. The fourth column—prefixed by the lowercase letter "p" for "pairs"—specifies the number of lone electron pairs. The fifth column—prefixed by the lowercase letter "c" for "charge"—specifies the formal charge on the atom. Bracketed values specify the presence of a bond, with the first value (i.e., number) indicating the index of the atom to which the current atom is bonded, and the second value (i.e., the uppercase letter) denoting the bond order: "S" for single, "D" for double, "T" for triple, or "B" for benzene-type bonds. If the molecule has an overall spin multiplicity (i.e., the degeneracy of the electronic ground state) larger than 1, it will be defined above the adjacency list (e.g., see the methoxy radical case in Figure 2). In the adjacency list of the methoxy radical molecule shown on the right-hand side of Figure 2, the oxygen atom has a single unpaired electron (thus having an overall spin multiplicity of 2) and one single bond to the carbon atom that has three single bonds to hydrogen atoms, forming a methoxy radical. After sorting out newly generated species and reactions by RMG using the adjacency lists method, we found that 65 species (indicated with the footnote *b* in Table 1) were included in both the RMG-generated network and the original EPACRIS library, with 40 new species generated by RMG, as shown in Table 2. We included nonreactive species, helium and neon, and 20 additional chemical species (indicated with the footnote *d* in Table 1), as well as their other relevant thermochemical reactions imported from the original EPACRIS reaction library in the photochemical network. We found that the species that were not included in the RMG-generated list (i.e., thermochemically not important) are mostly associated with photodissociation (e.g., $O(^1D)$) and the chemical network enabled by photodissociation. Consequently, we included them in our analysis to account for the impacts of photochemistry and aerosol chemistry, which might be significant in the atmospheres of WASP-39 b and WASP-80 b, except for the molecules that have more carbon atoms than C_3 hydrocarbons. Although C_3 and larger species are observed in Titan's atmosphere and mainly formed through photochemistry (Yung et al. 1984), we omitted them here due to the unfavorable physical (high-temperature) and chemical conditions (H_2-dominated) in hot Jupiters and the uncertainties in the relevant photodissociation rates. As a result, the final photochemical network contained 126 species and 2578 reactions (693 original reactions = 71 photochemistry reactions + 529

Table 1
111 Molecular Species Originally Included in the EPACRIS Library

Species	SMILES[a]	Species	SMILES[a]	Species	SMILES[a]
O[b]	[O]	O3[d]	[O-][O+] = O	H[b]	[H]
OH[b]	[OH]	HO2[b]	[O]O	H2O2[b]	OO
H_2O[b]	O	N[b]	[N]	NH_3[b]	N
NH_2[b]	[NH2]	N2O[b]	[N-] = [N+] = O	NO[b]	[N]=O
NO2[b]	[O-][N+] = O	NO3[d]	[O-][N+](= O)[O]	N2O5[d]	[O-][N+](=O)O[N+](=O)[O-]
HNO[b]	N = O	HNO2[b]	[O-][NH+] = O	HNO3[d]	[O-][N+](=O)O
C[b]	[C]	CO[b]	[C-]#[O+]	CH_4[b]	C
CH2O[b]	C = O	CH2O2[b]	O=CO	CH_3OH[b]	CO
CH3OOH[d]	COO	C2[d]	[C]#[C]	C2H2[b]	C#C
C2H3[b]	[CH]=C	C2H4[b]	C = C	C2H5[b]	C[CH2]
C2H6[b]	CC	HCCO[b]	[CH]=C = O	CH2CO[b]	C = C = O
CH3CO[b]	C[C]=O	CH3CHO[b]	CC=O	C2H5O[d]	CC[O]
HCN[b]	C#N	CN[b]	[C]#N	NCO[b]	[O]C#N
S[b]	[S]	S_2[b]	[S][S]	SO[b]	[S][O]
SO_2[b]	O = S = O	SO3[b]	O = S(=O)=O	H_2S[b]	S
SH[b]	[SH]	HSO[b]	O=[SH]	HOSO[b]	O[S]=O
OCS[b]	O = C = S	CS[d]	[C-]#[S+]	CH_3S[b]	C[S]
CO_2[b]	O = C = O	H_2[b]	[H][H]	O_2[b]	[O][O]
N_2[b]	N#N	$O(^1D)$[d]	O[c]	NH[b]	[NH]
e CH[b]	[CH]	CH2[b]	[CH2]	CH_3[b]	[CH3]
HCO[b]	[CH]=O	CH_3O[b]	C[O]	HOCO[b]	O=[C]O
C2H[b]	[C]#C	CH3NO2[d]	[O-][N+](=O)C	CH3NO3[d]	[O-][N+](=O)OC
CH2CN[b]	C = C=[N]	HOSO2[b]	[O]S(=O)O	CH_3SH[b]	CS
HNO4[d]	[O-][N+](=O)OO	CH3OO[b]	CO[O]	HNCO[b]	N = C = O
H2SO4[d]	OS(=O)(=O)O	$^1SO_2$[d]	[O]S[O][c]	$^3SO_2$[d]	[O]S[O]
S_3[d]	S = S = S	S_4[d]	S = S = S = S	H2SO4(A)[d]	aerosol
S_8[d]	S1SSSSSSS1	$^1CH2$[b]	[CH2][c]	C3H2	[CH]C#C
H_2CCCH	[CH]=C = C	H3CCCH	C#CC	H2CCCH2	C = C = C
C_3H_5	[CH2]C = C	C3H6	C=CC	C3H7	[CH2]CC
C_3H_8	CCC	C4H	[C]#CC#C	C4H2	C#CC#C
C_4H_3	[CH]=CC#C	C4H4	C#CC=C	C4H5	C=[C]C = C
CH_3CH_2CCH	C#CCC	CH3CHCCH2	C = C=CC	CH2CHCHCH2	C=CC=C
C_4H_8	C=CCC	C4H9	[CH2]CCC	C4H10	CCCC
C_6H	[C]#CC#CC#C	C6H2	C#CC#CC#C	C6H3	C#CC#C[C]=C
C_6H_6	c1ccccc1	C8H2	C#CC#CC#CC#C	CMHA	OCC1OC(O)C(O)C(O)C1O
N_2H_2[b]	N = N	N2H3[b]	[NH]N	N_2H_4[b]	NN
CH_3NH_2[b]	CN	CH3CHNH	CC=N	S_8(A)[d]	Aerosol

Notes.
[a] Simplified molecular-input line-entry system.
[b] A total of 65 chemical species that were included in the original EPACRIS library and were also picked by RMG to be important for describing the atmospheric conditions of WASP-39 b and WASP-80 b.
[c] Despite appearing as other chemical species or different spin states in the SMILES representation, these species are singlets in the adjacency lists representation, indicating all electrons are paired.
[d] A total of 20 chemical species additionally included in the photochemical network to fully account for photochemistry and aerosol chemistry that might be important in the atmospheres of WASP-39 b and WASP-80 b.

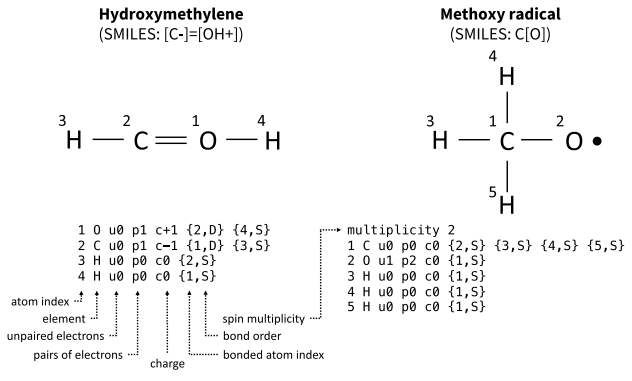

Figure 2. Adjacency list representations of hydroxymethylene (left) and methoxy radical (right). SMILES stands for simplified molecular-input line-entry system.

bimolecular reactions + 58 termolecular reactions + 35 thermodissociation reactions, and 1885 reactions newly generated by RMG). Except for the 71 photochemistry reactions, the other 2484 reactions are forward–reverse reaction pairs. In the future, we will incorporate only the thermal-driven reaction rate coefficients that are generated by RMG and only the photochemical reaction rate coefficients that are stored in the original reaction list into 1D kinetic-transport modeling.

2.3. Converting CHEMKIN Format to EPACRIS-readable Format

After automatic chemical network generation by RMG, as described in Section 2.1, the thermodynamic parameters (i.e., heat capacity, enthalpy, and entropy) and rate coefficients are provided in both CHEMKIN and Cantera (Goodwin et al. 2021)

Table 2
40 Newly Included Molecular Species in the Chemical Network Tailored for H_2-dominated Atmospheres by RMG

Species	SMILES[a]	Species	SMILES[a]
CH_2OH	[CH2]O	HCOH	[C-]=[OH+]
CH_2CHO	[CH2]C = O	H_2CC	[C]=C
CHCHO	[CH]=C[O]	c C_2H_3O	[CH]1CO1
OCHCO	O=[C]C = O	$HOCH_2O$	[O]CO
OCHO	[O]C = O	HSO_2	O=[SH]=O
HOS	O[S]	S a	[S][b]
HSS	S=[SH]	HSSH	SS
CH_2SH	[CH2]S	HCCS	[S]C#C
H_2SS	S=[SH2]	H_2CN	C=[N]
C_2N_2	N#CC#N	CH_3CN	CC#N
CH_2NH	C = N	NCOH	OC#N
NNH	[N]=N	NH2NO	NN=O
HNOH	[NH]O	HONO	ON=O
H_2NO	N[O]	NH2OH	NO
H_2NONO	NON=O	HNO(T)	[NH][O]
CH_3NH	C[NH]	CH_2NH_2	[CH2]N
CHNH	[CH]=N	HNC-2	[C-]#[NH+]
NCCN	[N]=C = C=[N]	H_2NCHO	NC=O
H_2NCO	N[C]=O	CH_3CHN	CC=[N]
C_2H_5CO	CC[C]=O	NH-2	[NH][b]

Notes.
[a] Simplified molecular-input line-entry system.
[b] Despite appearing as doublet or triplet radicals in the SMILES representation, these species are singlets in the adjacency lists representation, indicating all electrons are paired.

formats. The RMG-EPACRIS adapter then imports this information and converts it into a format adopted by EPACRIS to generate inputs to the 1D photochemical kinetic-transport atmospheric models, as described in the following Sections 2.3.1 and 2.3.2.

2.3.1. Thermodynamic Parameters

RMG uses the NASA polynomial representation (McBride & Gordon 1992) to calculate the relevant thermodynamic parameters. The NASA polynomial representation was originally developed by scientists at NASA to express temperature-dependent thermodynamic parameters, such as the heat capacity $C_p(T)$, enthalpy $H(T)$, and entropy $S(T)$, using seven or nine coefficients (McBride & Gordon 1992). In this representation, the following thermodynamic parameters are given by nine polynomial coefficients $a = [a_{-2}, a_{-1}, a_0, a_1, a_2, a_3, a_4, a_5, a_6]$ ($a_{-2} = a_{-1} = 0$ in the seven-coefficient version):

$$C_p(T) = R(a_{-2}T^{-2} + a_{-1}T^{-1} + a_0 + a_1T + a_2T^2 + a_3T^3 + a_4T^4), \quad (3)$$

$$H(T) = R(-a_{-2}T^{-1} + a_{-1}\ln T + a_0T + \frac{1}{2}a_1T^2 + \frac{1}{3}a_2T^3 + \frac{1}{4}a_3T^4 + \frac{1}{5}a_4T^5 + a_5), \quad (4)$$

$$S(T) = R(-\frac{1}{2}a_{-2}T^{-2} - a_{-1}T^{-1} + a_0\ln T + a_1T + \frac{1}{2}a_2T^2 + \frac{1}{3}a_3T^3 + \frac{1}{4}a_4T^4 + a_6). \quad (5)$$

Then the RMG-EPACRIS adapter obtains each species' Gibbs free energy, G, by the following equation:

$$G(T) = H(T) - TS(T). \quad (6)$$

The Gibbs free energy of species is used to calculate the reverse reaction rates in 1D photochemical kinetic-transport models using the methods outlined in Hu & Seager (2014).

2.3.2. Rate Coefficient Expressions

RMG adopts eight types of expressions for reaction rate constants. The RMG-EPACRIS adapter converts these into the formats adopted by EPACRIS (available in the supplementary .tar.gz archive), enabling the importation of the rate constants, k, for 1D kinetic-transport atmospheric modeling. Consequently, EPACRIS implements the same eight rate coefficient expressions, as elaborated below.

(1) The *Arrhenius*-type expression (Type 1) is an Arrhenius-type expression whose temperature-dependent rate coefficient, $k(T)$, follows the Arrhenius equation as shown in Equation (7):

$$k(T) = A\left(\frac{T}{T_0}\right)^n \exp\left(-\frac{E_a}{RT}\right). \quad (7)$$

In the Arrhenius equation, A represents the pre-exponential factor, T_0 the reference temperature in kelvins [K], n the temperature exponent, and E_0 the activation energy in joules per mole [J mol^{-1}]. Here, T denotes the temperature [K] and R is the ideal gas constant, 8.314 [J mol^{-1} K^{-1}]. The unit of A depends on the reaction order—[s^{-1}] for first-order reactions (i.e., unimolecular reactions, an elementary reaction in which the rearrangement of a single reactant produces one or more products), [m^3 mol^{-1} s^{-1}] for second-order reactions (i.e., bimolecular reactions, involving the simultaneous collision of any combination of two reactants), and [m^6 mol^{-2} s^{-1}] for third-order reactions (i.e., termolecular reactions, an elementary reaction involving the simultaneous collision of any combination of three reactants).

(2) The *multi-Arrhenius*-type expression (Type 2) is a multi-Arrhenius-type expression whose temperature-dependent rate coefficient, $k(T)$, follows a set of Arrhenius equations summed to obtain the overall rate coefficient, as shown in Equation (8):

$$k(T) = \sum_i A_i\left(\frac{T}{T_{0,i}}\right)^{n_i} \exp\left(-\frac{E_{a,i}}{RT}\right). \quad (8)$$

In the multi-Arrhenius equation, the index i refers to the ith set of Arrhenius parameters, which are consistent with those outlined in Equation (7).

(3) The *Pdep-Arrhenius-type expression* (Type 3), a Pdep-Arrhenius-type expression, defines the rate coefficient $k(T, P)$ as temperature- and pressure-dependent, formulated through either Arrhenius (i.e., Type 1) or multi-Arrhenius (i.e., Type 2) equations over multiple pressures

(see Equation (9)):

$$k(T, P) = A(P)\left(\frac{T}{T_0}\right)^{n(P)} \exp\left(-\frac{E_a(P)}{RT}\right)$$

or

$$k(T, P) = \sum_i A_i(P)\left(\frac{T}{T_{0,i}}\right)^{n_i(P)} \exp\left(-\frac{E_{a,i}(P)}{RT}\right). \quad (9)$$

The rate coefficients are then determined by log-scale interpolation between these expressions at each pressure. For example, the rate at an intermediate pressure $P_1 < P < P_2$ is computed as

$$\log k(T, P) = \log k(T, P_1) + \log\left(\frac{k(T, P_2)}{k(T, P_1)}\right)\frac{\log P - \log P_1}{\log P_2 - \log P_1}. \quad (10)$$

In the Pdep-Arrhenius equation, P refers to pressure [Pa]. $A(P)$ represents the pressure-dependent pre-exponential factor, $n(P)$ the pressure-dependent temperature exponent, and $E_0(P)$ the pressure-dependent activation energy in joules per mole [J mol^{-1}]. The unit of $A(P)$ depends on the reaction order—[s^{-1}] for first-order reactions, [m^3 mol^{-1} s^{-1}] for second-order reactions, and [m^6 mol^{-2} s^{-1}] for third-order reactions. The index i refers to the ith set of Arrhenius parameters. For pressures beyond the specified range, that is, $P \leqslant P_{\text{lowest}}$ or $P \geqslant P_{\text{highest}}$, the rate coefficient is determined by the Arrhenius equation at P_{lowest} for lower-pressure values and at P_{highest} for higher-pressure values.

(4) The *multi-Pdep-Arrhenius*-type expression (Type 4) is a multi-Pdep-Arrhenius-type expression that defines the rate coefficient $k(T, P)$ as temperature- and pressure-dependent, formulated through both Arrhenius (i.e., Type 1) and multi-Arrhenius (i.e., Type 2) equations (see Equation (11)):

$$k(T, P) = A(P)\left(\frac{T}{T_0}\right)^{n(P)} \exp\left(-\frac{E_a(P)}{RT}\right)$$

and

$$k(T, P) = \sum_i A_i(P)\left(\frac{T}{T_{0,i}}\right)^{n_i(P)} \exp\left(-\frac{E_{a,i}(P)}{RT}\right). \quad (11)$$

The rate coefficients are then determined by log-scale interpolation between these expressions at each pressure, as described in Equation (10). In the multi-Pdep-Arrhenius equation, all terms are consistent with those defined in the Pdep-Arrhenius-type expression (Type 3). Unlike the Pdep-Arrhenius-type expression, which formulates the rate coefficient exclusively as either Type 1 or Type 2, the multi-Pdep-Arrhenius-type expression offers a less consistent approach. In this equation, the rate coefficient expression can vary among Type 1 and Type 2, thus presenting a mixed format.

(5) The *third-body*-type expression (Type 5) is a third-body-type expression whose kinetics simply introduces an inert third body to the rate expression, as shown in Equation (12):

$$k(T, P) = k_0(T)[M]$$
$$k_0(T) = A\left(\frac{T}{T_0}\right)^n \exp\left(-\frac{E_a}{RT}\right)$$
$$[M] = \frac{P}{RT}. \quad (12)$$

In the third-body equation, $k_0(T)$ refers to the low-pressure-limit temperature-dependent rate coefficient. Its unit depends on the reaction order—[m^3 mol^{-1} s^{-1}] for first-order reactions and [m^6 mol^{-2} s^{-1}] for second-order reactions. $[M]$ is the concentration of the bath gas [mol m^{-3}].

(6) The *Lindemann*-type expression (Type 6) is a Lindemann-type expression that qualitatively models the falloff behavior of pressure-dependent reactions, as shown in Equation (13):

$$k(T, P) = k_\infty(T)\left[\frac{P_r}{1 + P_r}\right]$$
$$P_r = \frac{k_0(T)}{k_\infty(T)}[M]$$
$$k_0(T) = A_0\left(\frac{T}{T_{0,0}}\right)^{n_0} \exp\left(-\frac{E_{a,0}}{RT}\right)$$
$$k_\infty(T) = A_\infty\left(\frac{T}{T_{0,\infty}}\right)^{n_\infty} \exp\left(-\frac{E_{a,\infty}}{RT}\right). \quad (13)$$

In the Lindemann-type equation, the Arrhenius expressions (i.e., Type 1) k_0 and k_∞ represent the low-pressure and high-pressure limit kinetics, respectively. The units of k_0 and k_∞ vary with reaction order: for first-order reactions, they are [m^3 mol^{-1} s^{-1}] and [s^{-1}], and for second-order reactions, they are [m^6 mol^{-2} s^{-1}] and [m^3 mol^{-1} s^{-1}].

(7) The *Troe*-type expression (Type 7) is a Troe-type expression that quantitatively models the falloff behavior of pressure-dependent reactions by introducing a broadening factor F to the Lindemann equation, as shown in Equation (14):

$$k(T, P) = k_\infty(T)\left[\frac{P_r}{1 + P_r}\right]F$$
$$P_r = \frac{k_0(T)}{k_\infty(T)}[M]$$
$$k_0(T) = A_0\left(\frac{T}{T_{0,0}}\right)^{n_0} \exp\left(-\frac{E_{a,0}}{RT}\right)$$
$$k_\infty(T) = A_\infty\left(\frac{T}{T_{0,\infty}}\right)^{n_\infty} \exp\left(-\frac{E_{a,\infty}}{RT}\right). \quad (14)$$

The broadening factor F is computed via following

Equation (15):

$$\log F = \left\{1 + \left[\frac{\log P_r + c}{n - d(\log P_r) + c}\right]^2\right\}^{-1} \log F_{\text{cent}}$$
$$c = -0.4 - 0.67 \cdot \log F_{\text{cent}}$$
$$n = 0.75 - 1.27 \cdot \log F_{\text{cent}}$$
$$d = 0.14$$
$$F_{\text{cent}} = (1 - \alpha)\exp\left(\frac{-T}{T_3}\right) + \alpha \exp\left(\frac{-T}{T_1}\right) + \exp\left(\frac{-T_2}{T}\right). \quad (15)$$

In the Troe-type equation, the Arrhenius expressions (i.e., Type 1) k_0 and k_∞ represent the low-pressure and high-pressure limit kinetics, respectively. The units of k_0 and k_∞ vary with reaction order: for first-order reactions, they are [$m^3\,mol^{-1}\,s^{-1}$] and [s^{-1}], and for second-order reactions, they are [$m^6\,mol^{-2}\,s^{-1}$] and [$m^3\,mol^{-1}\,s^{-1}$]. Four parameters (i.e., α, T_1, T_2, and T_3) are provided to calculate the broadening factor F.

(8) The *Chebyshev*-type expression (Type 8) is a Chebyshev-type expression that adopts the Chebyshev polynomial formulation as a means of fitting a wide range of complex $k(T, P)$ behavior, as shown in Equation (16):

$$\log k(T, P) = \sum_{t=1}^{N_T} \sum_{p=1}^{N_P} \alpha_{tp} \phi_t(\widetilde{T}) \phi_p(\widetilde{P})$$
$$\widetilde{T} = \frac{2T^{-1} - T_{\min}^{-1} - T_{\max}^{-1}}{T_{\max}^{-1} - T_{\min}^{-1}}$$
$$\widetilde{P} = \frac{2\log P - \log P_{\min} - \log P_{\max}}{\log P_{\max} - \log P_{\min}}$$
$$\boldsymbol{\alpha} = \begin{bmatrix} \alpha_{11} & \alpha_{12} & \cdots & \alpha_{1N_P} \\ \alpha_{21} & \alpha_{22} & \cdots & \alpha_{2N_P} \\ \vdots & \vdots & \ddots & \vdots \\ \alpha_{N_T 1} & \alpha_{N_T 2} & \cdots & \alpha_{N_T N_P} \end{bmatrix}. \quad (16)$$

In the Chebyshev-type equation, α_{tp} are the constants defining the rate coefficient, and $\phi_n(x)$ is the Chebyshev polynomial of the first kind of degree n evaluated at x. The first few Chebyshev polynomials of the first kind are described in Equation (17):

$$\phi_n(x) \rightarrow \phi_1(x) = 1$$
$$\phi_2(x) = x$$
$$\phi_3(x) = 4x^3 - 3x$$
$$\phi_4(x) = 8x^4 - 8x^2 + 1$$
$$\phi_5(x) = 16x^5 - 20x^3 + 5x$$
$$\phi_6(x) = 32x^6 - 48x^4 + 18x^2 - 1$$
$$\vdots \quad (17)$$

$\widetilde{T}$ and $\widetilde{P}$ represent the reduced temperature and reduced pressures, respectively, mapping the ranges ($T_{\min}$, $T_{\max}$) and ($P_{\min}$, $P_{\max}$) to the interval (−1, 1). The Chebyshev rate expression is defined by the coefficient matrix $\boldsymbol{\alpha}$, comprising α_{tp} and specific temperature and pressure ranges, typically involving six values for temperature (i.e., $N_T = 6$) and four for pressure (i.e., $N_P = 4$). It is important to note that Chebyshev polynomials are only defined within the interval (−1, 1). Therefore, extrapolating rates beyond the defined temperature and pressure ranges is strongly discouraged, as the polynomials do not provide valid results outside these limits.

2.4. 1D Photochemical Kinetic-transport Atmospheric Modeling Using EPACRIS

After generating the chemical network with RMG for the conditions relevant to the H_2-dominated atmospheres of warm and hot Jupiters whose equilibrium temperatures are 800–1500 K (Section 2.1) and adapting it for EPACRIS using the RMG-EPACRIS adapter (Sections 2.2 and 2.3), we performed 1D photochemical kinetic-transport atmospheric modeling with EPACRIS to simulate the steady-state mixing ratio of chemical species in the atmospheres of WASP-39 b and WASP-80 b. The photochemical kinetic-transport module of EPACRIS was employed to calculate the steady-state chemical composition of WASP-39 b's atmosphere of each morning and evening terminator (following Tsai et al. 2023) and that of WASP-80 b's atmosphere (following Bell et al. 2023), considering thermochemical equilibrium, vertical transport, and photochemical processes. We assumed cloud-free conditions and zero-flux boundary conditions. The temperature–pressure profiles (Figure 3(a)), the eddy diffusion coefficient profiles (Figure 3(b)), and the stellar spectra (Figure 3(c)) are adopted from Bell et al. (2023) and Tsai et al. (2023). In the case of WASP-80 b, we used the stellar flux of HD 85512 (K6V) at 1 au distance, adopted from the MUSCLES survey III (Loyd et al. 2016). It should be noted that the stellar spectrum significantly influences the photolysis rates. From this, one can intuitively infer that the atmospheric chemistry of WASP-39 b is more significantly impacted by photochemistry compared to that of WASP-80 b, based on Figure 3(c), which shows that the stellar flux on WASP-39b is 10–100 times stronger than that on WASP-80 b. We assumed atmospheric abundances of 10× solar metallicity (Lodders 2020) for both WASP-39 b (Rustamkulov et al. 2023; Tsai et al. 2023) and WASP-80 b (Bell et al. 2023). These choices facilitate a direct comparison between the EPACRIS-simulated WASP-39 b and WASP-80 b atmospheres and published results. After the model has converged and reached the steady state, we compute the synthetic transmission spectra of WASP-39 b and WASP-80 b based on the molecular mixing ratio profiles (Figures 4 and 8), using the transmission spectra generation module of EPACRIS (Hu et al. 2013), and compare the resulting transmission spectra with JWST observations (Bell et al. 2023; Rustamkulov et al. 2023; Powell et al. 2024).

3. Results and Discussions

3.1. WASP-39 b

3.1.1. Overall Behavior of Main Sulfur-bearing Species in the Atmosphere of WASP-39b

Figure 4 shows the comparison between the previously reported vertical molecular mixing ratio profiles of major species and those simulated from the current work using EPACRIS. As shown in Figure 4, the vertical mixing ratios of all species at pressures higher than $\sim 10^2$ mbar are consistent across all five models, including EPACRIS and four others in Tsai et al. (2023). This consistency suggests that the deep atmospheric chemistry of WASP-39b is primarily governed by thermal chemistry, which excludes photochemistry, and aligns with thermochemical equilibrium, as depicted in Figure A1. The minor variations in the behaviors of SH and S_2 are

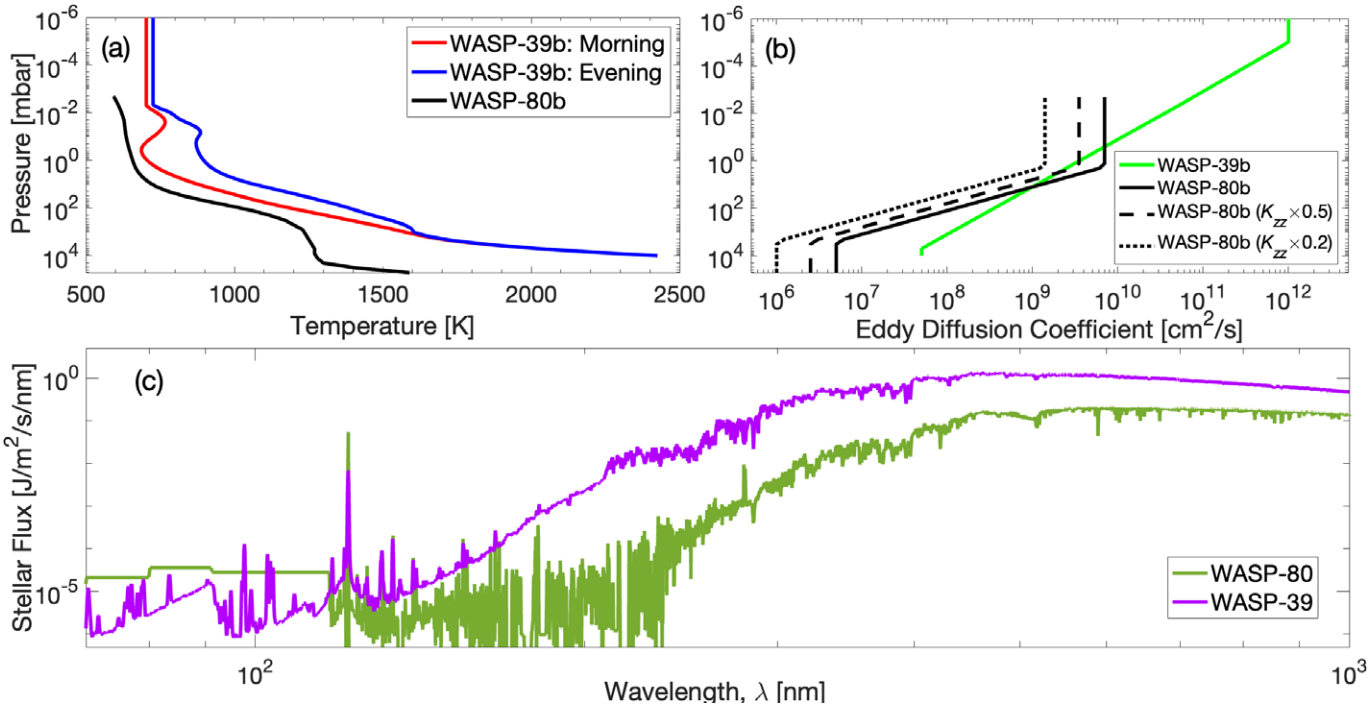

Figure 3. (a) Temperature–pressure profiles for the morning (red) and evening (blue) limbs for WASP-39 b and for WASP-80 b (black). (b) Eddy diffusion coefficient (K_{zz}) profile for WASP-39 b (lime) and WASP-80 b (black solid line), two times slower eddy diffusion coefficient profile for WASP-80 b (black dashed line), and five times slower eddy diffusion coefficient profile for WASP-80 b (black dotted line). (c) The stellar flux at 1 au distance for WASP-39 (purple) and WASP-80 (green). These input parameters are adopted from Tsai et al. (2023) and Bell et al. (2023), except for the stellar spectra of WASP-80. The stellar flux of HD 85512 (K6V) at 1 au distance, adopted from the MUSCLES survey III (Loyd et al. 2016), is used for WASP-80 b.

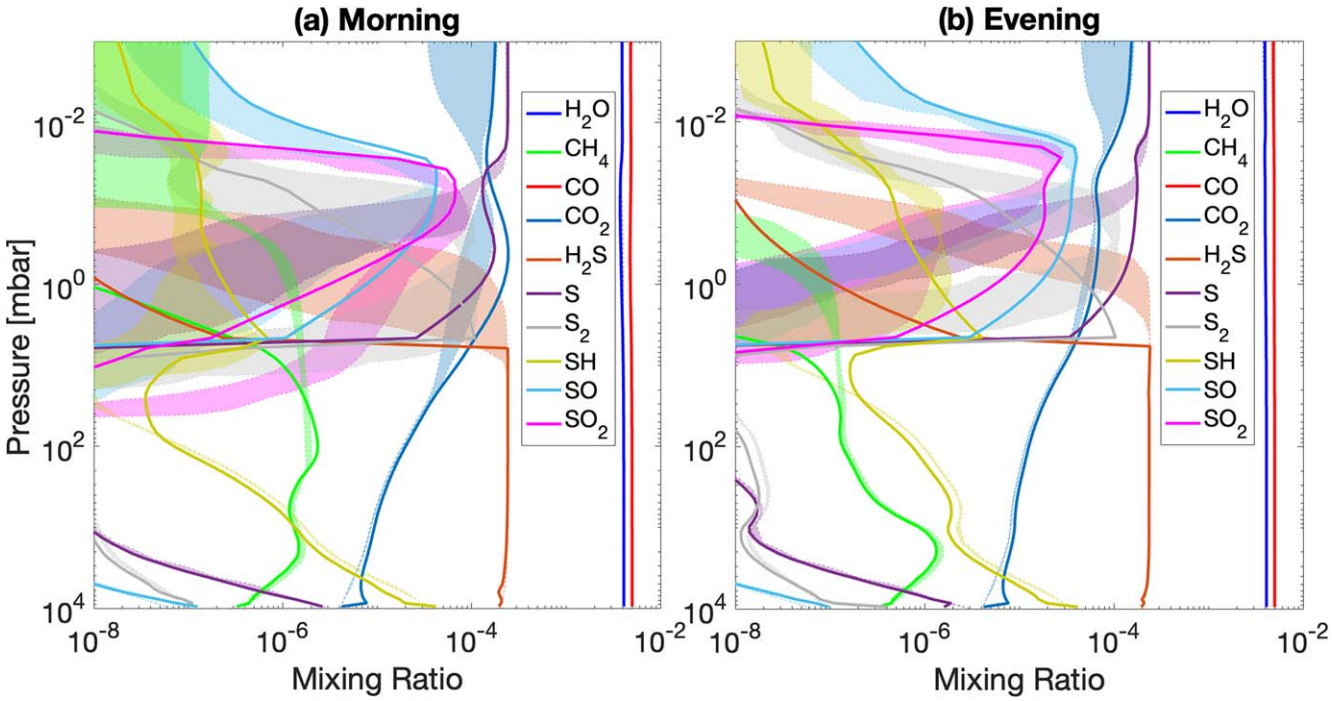

Figure 4. Comparison between the previously reported vertical molecular mixing ratio profile of major species simulated for the (a) morning and (b) evening terminators of WASP-39 b in Tsai et al. (2023; color-shaded areas) and those simulated from the current work using EPACRIS (solid lines). Each color indicates the corresponding species (SO_2: magenta; H_2O: blue; CH_4: green; CO: red; CO_2: dark blue; H_2S: brown; S: purple; S_2: gray; SH: yellow; and SO: light blue) and the color-shaded areas indicate the span enclosed by the photochemical models presented in Tsai et al. (2023).

primarily attributed to differences in the Gibbs free energy of these species. For example, VULCAN (Tsai et al. 2017, 2021), one of the models used in Tsai et al. (2023), utilizes thermodynamic parameters for SH and S_2 from Goos et al. (2016) and McBride et al. (2002). These sources calculated NASA polynomials based on the data from McBride et al. (2002). In contrast, RMG uses thermodynamic parameters for SH whose NASA polynomials are calculated by Song et al.

(2017), which are based on the data from Shiell et al. (2000) and, for S_2, from the NIST-JANAF table (Chase 1985). It is evident that each parameter in the photochemical modeling inherently contains a certain amount of uncertainties. Among these, in general, rate coefficients and thermodynamic parameters are the most significant contributors to the uncertainties of chemical kinetic models. Therefore, assessing the model's sensitivity to thermodynamic parameters as well as rate coefficients is of paramount importance when it comes to the preciseness of atmospheric photochemical modeling.

At pressures less than $\sim 10^2$ mbar (i.e., where photochemistry and vertical mixing become more significant), the EPACRIS simulations (solid lines in Figure 4) of the main sulfur species (H_2S, SH, S_2, S, SO, and SO_2) align closely with the models in Tsai et al. (2023). The peak mixing ratios of these species are generally within an order of magnitude of each other for both the morning and evening terminators, as illustrated in Figures 4(a) and (b). Although these models represent the atmospheric steady state, making it challenging to track the time-dependent chemical evolution, some insights can still be gleaned. For instance, in the deep atmosphere (around $\sim 10^4$ mbar), thermochemically favored H_2S (hydrogen sulfide) is the dominant sulfur-bearing species up to a pressure of about 10 mbar (at temperatures above 900 K), for both terminators. In addition to H_2S, sulfur monohydride (SH) is the second most abundant sulfur species in the deep atmosphere. Between 5 and 8 mbar, H_2S rapidly transitions to S_2 and S, with SO and SO_2 also present. Above 1 mbar, atomic sulfur (S) becomes the dominant sulfur species, with SO and SO_2 peaking at the maximum mixing ratio at $\sim 10^{-1}$–10^{-2} mbar for both the morning ($[SO]_{max} = \sim 42$ ppm, $[SO_2]_{max} = \sim 68$ ppm) and evening ($[SO]_{max} = \sim 40$ ppm, $[SO_2]_{max} = \sim 28$ ppm) terminators.

One notable difference between the current model (i.e., EPACRIS) and the models previously reported in Tsai et al. (2023) lies in the amounts of the SO_2 levels predicted between 0.5 and 10 mbar for both the morning and evening terminators of WASP-39b (see Figures 4(a) and (b)). In the morning terminator, Tsai et al. (2023) predicts SO_2 mixing ratios above 1 ppm (i.e., 10^{-6}), starting from around 10 mbar. In contrast, EPACRIS indicates this level is reached at around 2 mbar, a higher altitude (Figure 4(a)). Conversely, for the evening terminator, Tsai et al. (2023) suggest SO_2 exceeds 1 ppm, starting from 0.5 mbar, whereas EPACRIS shows this occurring at around 3 mbar, a lower altitude (Figure 4(b)). This increased formation of SO_2 on the evening side compared to the morning side is explained in Section 3.1.2. It has to be noted that the mixing ratio prediction at around 1 mbar is potentially significant for JWST observations in transmission, especially considering the NIRSpec mode's primary probing range of 0.1–2 mbar (Rustamkulov et al. 2023).

Another notable difference involves the amounts of the CH_4 levels predicted in the atmosphere above $P \sim 10$ mbar for both the morning and evening terminators (see Figures 4(a) and (b)). According to the thermochemical equilibrium vertical mixing ratio profile of CH_4 (as shown in Figure A1), the CH_4 mixing ratio at around 10 mbar should be more than 100 ppm in the morning terminator and more than 1 ppm in the evening terminator, but this is not the case, since the quenching kinetics starts to happen around 100 mbar for both the morning and evening terminators, followed by the photodissociation of CH_4 at higher altitude ($P \sim 1$ mbar), as shown in Figure 4. However, on top of this, the current model shows a more depleted CH_4 level compared to the previous modeling studies in Tsai et al. (2023), which indicates additional scavenging reactions for CH_4 sources (e.g., CH_3). According to the rate analysis, the reactions

$$\begin{aligned} CH_3 + S &\rightarrow CH_3S \\ CH_3 + SH &\rightarrow CH_3SH \end{aligned} \quad (18)$$

lead to continuous reactions forming various carbon and sulfur-bearing species, ultimately resulting in the depletion of methane. As pointed out in Tsai et al. (2023), sulfur can affect other nonsulfur species, including CH_4 (see the Extended Data in Figure 6 of Tsai et al. 2023), and the additional sulfur species listed in Table 2 (e.g., CH_2SH is not included in VULCAN or KINETICS, both of which were used in Tsai et al. 2023) and related reactions (e.g., $CH_3 + S \rightarrow CH_3S$ is not included in VULCAN; Tsai et al. 2023) in RMG-generated chemical networks are attributed to this additional CH_4 depletion in the upper atmosphere of WASP-39 b. This rapid drop of CH_4 abundance at around 1 mbar matches the rapid appearance of S and S_2 originating from the dissociation of H_2S (see Figure 4).

3.1.2. Various Origins of H and OH Radicals for the Formation of SO_2 in the Atmosphere of WASP-39 b

Generally, sulfur dioxide (SO_2) at high altitudes ($P \sim 10^{-2}$–0.5 mbar) is more prevalent at the cooler morning terminator of WASP-39b, whereas at lower altitudes ($P \sim 0.5$–10 mbar), SO_2 is more abundant at the hotter evening terminator. To understand this distribution pattern, it is crucial to track the origin of oxidizers (i.e., OH and H radicals), since the SO_2 in the atmosphere of WASP-39 b is mainly produced by the successive oxidation of sulfur species originating from the deep-atmosphere hydrogen sulfide (H_2S), as pointed out in the previous modeling work of Tsai et al. (2023).

As illustrated in Figure 5, the vertical molecular mixing ratios of both OH and H radicals display similar patterns, largely due to the dissociation of H_2O into H and OH. This also indicates that H_2O is a main source for OH as well as H. However, their magnitudes differ, with additional sources of H, such as H_2 and H_2S, contributing to these variations. The morning and evening vertical mixing ratio profiles of these species (i.e., OH and H radicals), as shown by the solid (morning) and dashed (evening) lines in Figure 5, cannot be fully explained by thermochemical equilibrium (dashed–dotted line for the morning and dotted line for the evening) alone. This discrepancy indicates that a combination of thermal chemistry, photochemistry, and vertical mixing influences these behaviors. Further analysis, as shown in Figure 6(a), indicates that the origins of OH radicals change with altitude (or pressure), suggesting a complex interplay of atmospheric processes at different levels. As shown in Figure 6(a), from the upper atmosphere at around 10^{-7} mbar down to 10^{-3} mbar, the reactions

$$H_2O \xrightarrow{h\nu} OH + H \quad (19)$$

$$OH + H_2 \rightarrow H_2O + H \quad (20)$$

serve as the major OH source and sink, respectively (rates $\sim \pm 2 \times 10^5$ [molecules cm^{-3} s^{-1}]).

Then, in between 10^{-3} and 10^{-1} mbar, the reactions

$$O + H_2 \rightarrow OH + H \quad (21)$$

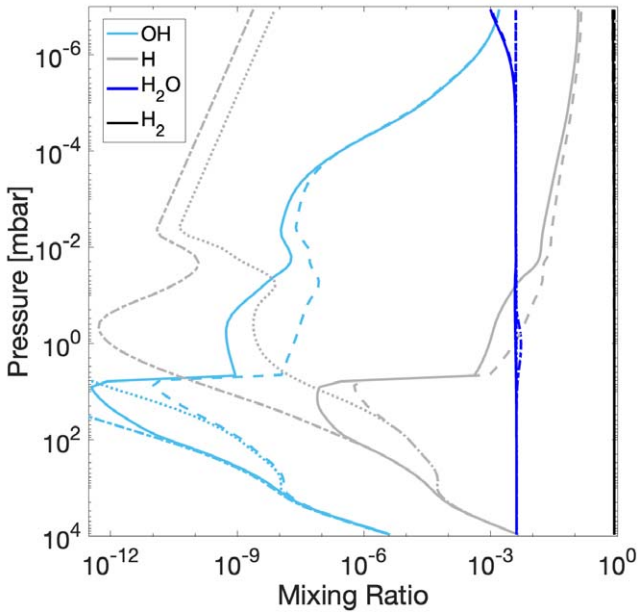

Figure 5. The vertical molecular mixing ratio profiles of several species (H_2, H_2O, H, and OH) simulated for the morning (solid lines) and evening (dashed lines) terminators of the WASP-39 b atmosphere. The thermochemical equilibrium vertical molecular mixing ratios are also indicated by the dashed–dotted lines (morning terminator) and dotted lines (evening terminator). Although not shown in the figure, the thermochemical equilibrium vertical molecular mixing ratios for the morning and evening terminators of OH show similar patterns to those of H radicals with a smaller amplitude by ∼6 orders of magnitude. Each color indicates the corresponding species (OH: light blue; H: gray; H_2O: blue; and H_2: black).

$$OH + S \rightarrow SO + H \tag{22}$$

serve as the major OH source and sink, respectively (rates $\sim \pm 3 \times 10^7$ [molecules cm^{-3} s^{-1}]). And, as shown in Figure 6(a), at the pressure between 10^{-1} and 10^1 mbar, the reactions

$$HSO + H \rightarrow OH + SH \tag{23}$$

$$OH + S \rightarrow SO + H \tag{24}$$

serve as the major OH source and sink, respectively (rates $\sim \pm 6 \times 10^9$ [molecules cm^{-3} s^{-1}]). The reaction rates get larger with decreasing altitude, since the molecular number density [molecules cm^{-3} s^{-1}] gets larger with decreasing altitude (i.e., increasing pressure $\propto$ number density). This interconversion of OH and H radicals is rapid, leading to the formation of a combined H + OH chemical group whose relative ratio remains constant under specific atmospheric conditions, as depicted in Figure 5.

As highlighted previously, water vapor (H_2O) is a primary source of these radicals. Rate analysis involving H_2O (Figure 6 (b)) shows that the formation of OH and H, crucial for SO_2 production, primarily occurs through two distinct reactions in different atmospheric regimes. In the upper atmosphere, at pressures below 10^{-2} mbar, H_2O photolysis is the predominant reaction (see Figures 6(a) and (b)). Conversely, in the middle atmosphere, within the pressure range of 1–10 mbar, the interaction between H_2O and sulfur radicals (originated from H_2S) becomes increasingly significant (as shown in Figure 6(b)). These interactions can be summarized by the following reactions:

$$\begin{aligned} &H_2S \rightarrow H_2 + S \\ &H_2O + S \rightarrow OH + SH \\ &SH + S \rightarrow H + S_2 \\ &S_2 \xrightarrow{h\nu} S + S \\ &\text{Net: } H_2S + H_2O \rightarrow H_2 + OH + H + S. \end{aligned} \tag{25}$$

This summarized scheme is consistent with the rapid increase in H and OH around 10 mbar, as shown in Figure 5, and the rapid depletion of H_2S along with a rapid increase in S at the same pressure level, as shown in Figures 4(a) and (b). It is also noteworthy that the thermochemical equilibrium mixing ratio of H_2O at pressures between 1 and 10 mbar is slightly higher than its vertical mixing ratio of H_2O (see Figure 5). The transport rate (vertical mixing) in this region (i.e., $P \sim 1$–10 mbar) was at least 2 orders of magnitude slower than the total loss rates. This suggests that vertical transport is not the predominant factor for the straight feature of the H_2O vertical mixing ratio profile at this region. Instead, this straight feature indicates that the decreased amount of H_2O in this region is being converted into H and OH, corroborating the above reaction scheme.

If we combine the $T - P$ profiles (see Figure 3(a)) with the OH vertical mixing ratios of the morning and evening terminators (the solid and dashed lines, respectively, in Figure 5), we can see the positive correlation between the OH (and H) radical mixing ratios and temperature within the 10^{-1}–10^1 mbar pressure range. Notably, in this range (i.e., 10^{-1}–10^1 mbar), the morning terminator consistently exhibits temperatures ∼200 K lower than the evening terminator. As described earlier, the origin of the lower-atmosphere OH is more thermally driven by chemistry and less driven by H_2O photolysis, and thus sensitive to temperatures. As a result, within the 10^{-1}–10^1 mbar pressure range, OH radicals are more than an order of magnitude more abundant in the hotter evening terminator compared to the cooler morning terminator, as illustrated in Figure 5. This increased OH abundance leads to more SO_2 formation at lower altitudes ($P \sim 0.5$–10 mbar) through OH-aided successive oxidation.

3.1.3. Theoretical Transmission Spectra of the Atmosphere of WASP-39 b Generated by EPACRIS

Figure 7 shows the comparison between the averaged theoretical transmission spectra generated by EPACRIS and JWST observations of WASP-39 b (Alderson et al. 2023; Feinstein et al. 2023; Powell et al. 2024). The EPACRIS-predicted transmission spectra are broadly consistent with the near- and mid-infrared observations. The model accurately captures the features of H_2O (blue), CO_2 (red), and SO_2 (magenta). While the CO (green) feature at 4.5–5 μm appears to be overpredicted, considering the uncertainties, the overall agreement between the model predictions and observations is still considered decent. The predicted transmission spectra generated by the previous photochemical networks, assuming 10× solar metallicity, as discussed in Tsai et al. (2023), align well with the NIRSpec/G395H spectra (Feinstein et al. 2023). However, they overpredict the transit depth in the 7–8 μm wavelength range, which corresponds to the dominant SO_2 absorption feature when compared to the MIRI data reported by Powell et al. (2024). Consequently, using the same photochemical networks resulted in the lowest χ^2 value of 2.51 when

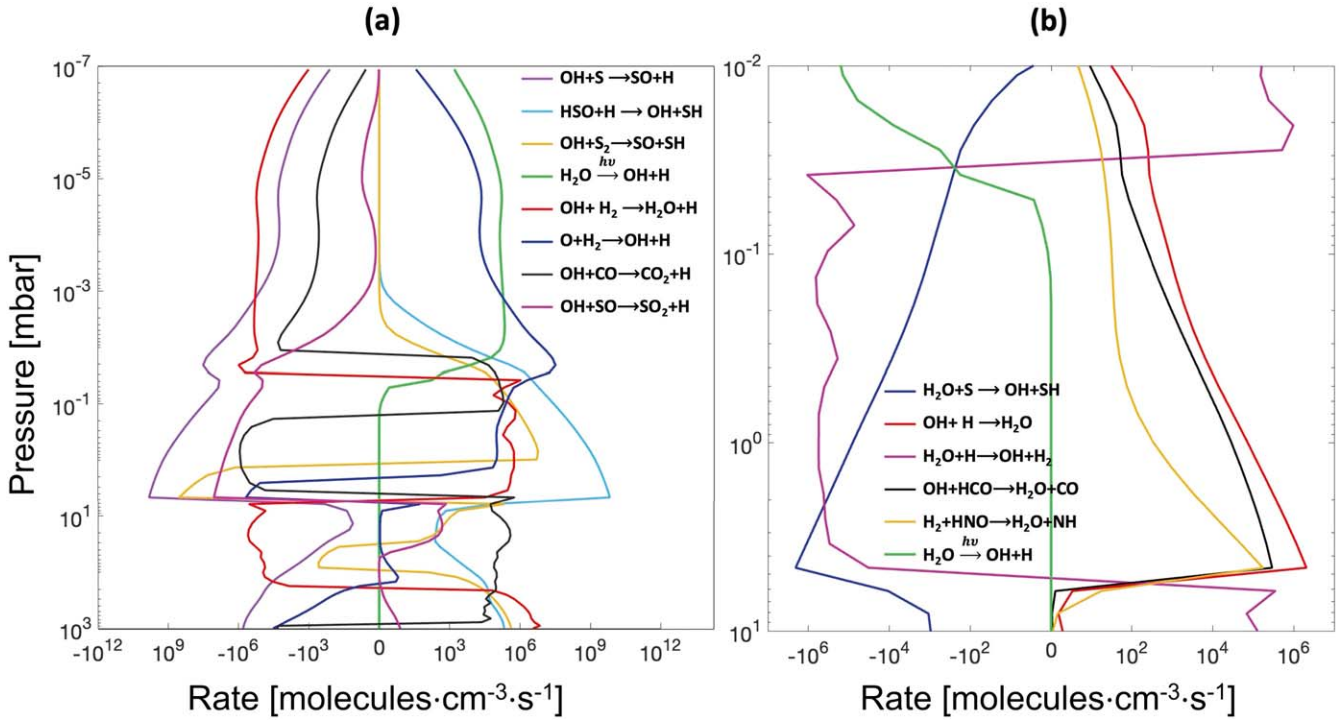

Figure 6. The rate–pressure profiles of dominant reactions involving specific chemical species in the morning terminator. (a) Rates of reactions involving OH radicals presented at pressure ranges between 10^{-7} and 10^{3} mbar. Among 318 OH-involved reactions, only eight dominant reactions are shown here, for readability. Each color of the solid lines indicates a corresponding reaction. Negative values in the rate indicate the reaction acts as a sink for OH species, while positive values indicate the reaction serves as a source for OH species. The rate–pressure profile for the evening terminator exhibited behavior similar to that of the morning terminator, with the primary difference being in the amplitudes of the rates (the evening rates are in general slightly faster within a factor of 2–3). Due to this similarity, the evening profile is not separately illustrated. (b) Reactions involving H_2O, presented at pressure ranges between 10^{-2} and 10 mbar. Among 124 H_2O-involved reactions, only six dominant reactions are shown here, for readability. Each solid line color corresponds to a specific reaction, with the colors representing the six rates in descending order, from largest to smallest. Negative values in the rate indicate the reaction consumes H_2O, while positive values indicate a reaction that produces H_2O. As mentioned in the main text, in the upper atmosphere, H_2O photolysis (lime) serves as a major source for OH species, while the $H_2O + S \rightarrow OH + SH$ reaction (blue) in the middle atmosphere at a pressure of 1–10 mbar serves as a major source for OH.

assuming 7.5× solar metallicity, while the χ^2 for 10× solar metallicity was 2.91 (Powell et al. 2024). In contrast, the predicted transmission spectra using the photochemical network from the current study showed an even lower χ^2 of 2.10. This network matches well with the NIRISS/SOSS, NIRSpec/G395H, and MIRI/LRS spectra, without the need to vary solar metallicity. As highlighted in the previous Section 3.1.1, the vertical mixing ratios of species in the 0.1–2 mbar pressure range are probed by JWST observations in transmission. Differences in the photochemical network can lead to significantly varied results in the vertical mixing ratio profiles, thus influencing the predicted transmission spectra.

3.2. WASP-80 b

3.2.1. Upper-atmosphere Chemistry Affected by Deep-interior Thermochemistry and Quenching Kinetics

WASP-80 b's equilibrium temperature ($T_{eq} = 825$ K; Triaud et al. 2015) is approximately 300 K cooler than WASP-39 b's (T_{eq}=1116 K, Faedi et al. 2011). This suggests that transport-induced quenching, where the lifetime of the chemical species becomes longer relative to the vertical mixing timescale, could play a more significant role in the cooler atmosphere of WASP-80 b compared to the hotter WASP-39 b. Figure 8 illustrates that all major species, including H_2O, CO, CH_4, NH_3, and HCN, originate from the deep interior (the quenching point is at around $P = 10^3$ mbar) and are transported to the upper atmosphere, where some species, such as CH_4 and NH_3, undergo photodissociation. Notably, the model-predicted H_2O volume mixing ratio aligns well with the JWST observations (Bell et al. 2023) as well as the CH_4 prediction. Although other major species, such as NH_3, HCN, CO_2, CO, and SO_2, were not constrained from the observations, all these model-predicted mixing ratios fall within the upper-limit values derived from emission and transmission spectra, except an SO_2 upper limit determined from emission spectra (see the magenta left-pointing triangle symbol in Figure 8).

As expected, the CH_4 mixing ratio as well as other species (e.g., NH_3 and HCN) formed from deep-interior thermochemistry are sensitive to quenching kinetics. As depicted in Figure 8, the black solid and dashed lines represent the CH_4 volume mixing ratio using eddy diffusion coefficient (K_{zz}) profiles that are two times slower and five times slower, respectively, than the K_{zz} profile adopted from Bell et al. (2023; see Figure 3(b)). When using these slower K_{zz} profiles, the predicted CH_4 mixing ratio becomes more consistent with the observational constraints while not changing the predicted H_2O mixing ratio, and the NH_3 and HCN mixing ratios shift to lower mixing ratios, indicating a shift of the deep-interior quenching point toward lower pressure (see Figure 8). Consequently, more detailed constraints on other species, such as CO_2, NH_3, CO, and SO_2, are required to precisely describe WASP-80 b's atmospheric chemistry. Despite the uncertainties in metallicity and the K_{zz} profile, the current model aligns reasonably well with the observational data, providing valuable insights into the atmospheric behavior of this exoplanet.

3.2.2. Detailed Chemistry and Newly Suggested Deep-interior Nitrogen Incorporation Pathway

As shown in Figure 10(a), the deep-interior CO–CH_4 conversion is

$$\begin{aligned} \mathrm{CO + H} &\xrightarrow{\mathrm{M}} \mathrm{HCO} \\ \mathrm{HCO + H_2} &\rightarrow \mathrm{CH2O + H} \\ \mathrm{CH_2O + H} &\xrightarrow{\mathrm{M}} \mathrm{CH_2OH} \\ \mathrm{CH_2OH + H_2} &\rightarrow \mathrm{CH_3OH + H} \\ \mathrm{CH_3OH} &\xrightarrow{\mathrm{M}} \mathrm{CH_3 + OH} \\ \mathrm{CH_3 + H_2} &\rightarrow \mathrm{CH_4 + H} \\ \mathrm{Net:\ CO + 3H_2} &\rightarrow \mathrm{CH_4 + H_2O}, \end{aligned} \tag{26}$$

with M representing any third-body molecule. This scheme is identical to scheme (1) in Moses et al. (2016). The SO_2 formation mechanism in the upper atmosphere predicted in the model was similar to the SO_2 formation in the atmosphere of WASP-39 b previously described in Section 3.1.2. The CO_2 formation mechanism was the combination of deep-interior CO_2 formation and the additional oxidation of CO through OH radicals at the atmosphere above $P \sim 1$ mbar.

Figure 10(b) visualizes the N_2 to NH_3 to HCN conversion pathway in the deep interior. This pathway mostly resembles those detailed in Moses et al. (2016), with a key difference in the initial incorporation of nitrogen from N_2 into species like NH_3 and HCN. The well-known $N_2 \rightarrow NH_3$ route, as outlined in Moses et al. (2016), involves multiple hydrogenation steps, starting with N_2 activation by a hydrogen atom to form NNH, ultimately yielding NH_3 as follows:

$$\begin{aligned} \mathrm{N_2 + H} &\xrightarrow{\mathrm{M}} \mathrm{NNH} \\ \mathrm{NNH + H_2} &\rightarrow \mathrm{N_2H_2 + H} \\ \mathrm{N_2H_2 + H} &\rightarrow \mathrm{NH + NH_2} \\ \mathrm{NH + H_2} &\rightarrow \mathrm{NH_2 + H} \\ \mathrm{2(NH_2 + H_2} &\rightarrow \mathrm{NH_3 + H)} \\ \mathrm{2H} &\xrightarrow{\mathrm{M}} \mathrm{H_2} \\ \mathrm{Net:\ N_2 + 3H_2} &\rightarrow \mathrm{2NH_3}. \end{aligned} \tag{27}$$

Despite this scheme being included in the RMG-generated chemical network for hot Jupiter exoplanet atmospheres described in Section 2.1, RMG suggests a different dominant deep-interior pathway for $N_2 \rightarrow NH_3$ conversion that initiates with N_2 directly interacting with two H_2 molecules to form N_2H_2, eventually leading to NH_3 (highlighted in Figure 10(b)), as in the following scheme:

$$\begin{aligned} &\mathrm{N_2 + H_2 + H_2} \rightarrow \mathrm{N_2H_2 + H_2} \\ &\mathrm{N_2H_2 + H_2} \rightarrow \mathrm{N_2H_4} \\ &\mathrm{N_2H_4} \rightarrow \mathrm{2NH2} \\ &\mathrm{2NH2 + 2H2} \rightarrow \mathrm{2NH_3 + 2H} \\ &\mathrm{2H} \xrightarrow{\mathrm{M}} \mathrm{H_2} \\ &\mathrm{Net:}\ N_2 + 3H_2 \rightarrow 2NH_3. \end{aligned} \tag{28}$$

In this scheme, N_2 is activated by two H_2 molecules, forming *cis*-N_2H_2 (see Figure 9). The transition state for this reaction was first identified by Asatryan et al. (2010) using the CBS-QB3 level of theory. In contrast to the simple bimolecular addition of N_2+H_2 with an initial barrier of 125 kcal mol^{-1} (calculated at the G2M(MP2)//MP2/6-31G** level of theory by Hwang & Mebel 2003), this dihydrogen-activated nitrogen fixation has a relatively much lower barrier of about 77 kcal mol^{-1} (Asatryan et al. 2010). While the initial barrier in Scheme (27) is lower (17.1 kcal mol^{-1}; Hwang & Mebel 2003), subsequent steps, such as NNH+$H_2 \rightarrow N_2H_2$+H, face much higher barriers (42 kcal mol^{-1}; Hwang & Mebel 2003), and Scheme (27) has to go through one more additional elementary reaction compared to Scheme (28). We tested the sensitivity of the photochemical model to the newly suggested reaction by intentionally disabling it. We found that under the conditions of WASP-80 b's atmosphere, the overall mixing ratio did not show significant changes. However, under certain favorable deep atmospheric conditions (e.g., hot and high-pressure conditions), this newly suggested N_2 incorporation step could lead to significantly greater formation of NH_3 or HCN species.

In this study, the rate coefficient for N_2+$2H_2\rightarrow N_2H_2$+H_2 is considered as a high-pressure limit, calculated via conventional transition state theory. However, as this termolecular reaction involves three actual reactants (unlike the usual third-body [*M*] considered as an unreacted agent), it is inherently pressure-dependent and entropically less favorable. Despite these, such reactions are likely viable under the high pressures characteristic of the deep-interior chemistry in hot Jupiter atmospheres, underscoring the importance of their inclusion for accurate nitrogen incorporation modeling. This case highlights the substantial advantages of systematic, computer-aided, automatic chemical network generation, which can reveal previously overlooked chemical pathways and provide detailed insights into exoplanet atmospheric chemistry.

As shown in Figure 10(b), the $NH_3 \rightarrow$ HCN conversion scheme at pressures between 10^3 and 10^4 mbar is

$$\begin{aligned} &\mathrm{NH_3 + H} \rightarrow \mathrm{NH_2 + H_2} \\ &\mathrm{CH_4 + H} \xrightarrow{\mathrm{M}} \mathrm{CH_3 + H_2} \\ &\mathrm{NH_2 + CH_3} \xrightarrow{\mathrm{M}} \mathrm{CH_3NH_2} \\ &\mathrm{CH_3NH_2 + H} \rightarrow \mathrm{CH_3NH\ (or\ CH_2NH_2) + H_2} \\ &\mathrm{CH_3NH\ (or\ CH_2NH_2)} \xrightarrow{\mathrm{M}} \mathrm{CH_2NH + H} \\ &\mathrm{CH_2NH + H} \rightarrow \mathrm{H_2CN\ (or\ CHNH) + H_2} \\ &\mathrm{H_2CN\ (or\ CHNH) + H} \rightarrow \mathrm{HCN + H_2} \\ &\mathrm{H_2} \xrightarrow{\mathrm{M}} \mathrm{H + H} \\ &\mathrm{Net:\ NH_3 + CH_4} \rightarrow \mathrm{HCN + 3H_2}. \end{aligned} \tag{29}$$

This pathway mostly resembles those detailed in Moses et al. (2016), with additional species (i.e., CH_3NH and CHNH are newly included species by RMG) and reactions (i.e., CH_3NH_2+H$\rightarrow CH_3NH$+H_2, $CH_3NH \xrightarrow{M} CH_2NH$+H, CH_2NH+H$\rightarrow$CHNH+H_2, and CHNH+H$\rightarrow$ HCN+H_2).

3.2.3. Theoretical Transmission Spectra of the Atmosphere of WASP-80 b Generated by EPACRIS

Figure 11 compares EPACRIS-generated theoretical transmission spectra with JWST NIRCam observations of WASP-80 b (Bell et al. 2023). The EPACRIS prediction aligns well with the NIRCam data ($\chi^2 = 1.748$ for Eureka! and 1.407 for tshirt), particularly in capturing the H_2O (blue) and CH_4 (green) features identified in Bell et al. (2023). Due to NIRCam's wavelength range limitations for CO_2 and SO_2 detection, comparing these species with model predictions is challenging. However, our model indicates that future JWST NIRSpec/G395H observations could potentially confirm the presence of

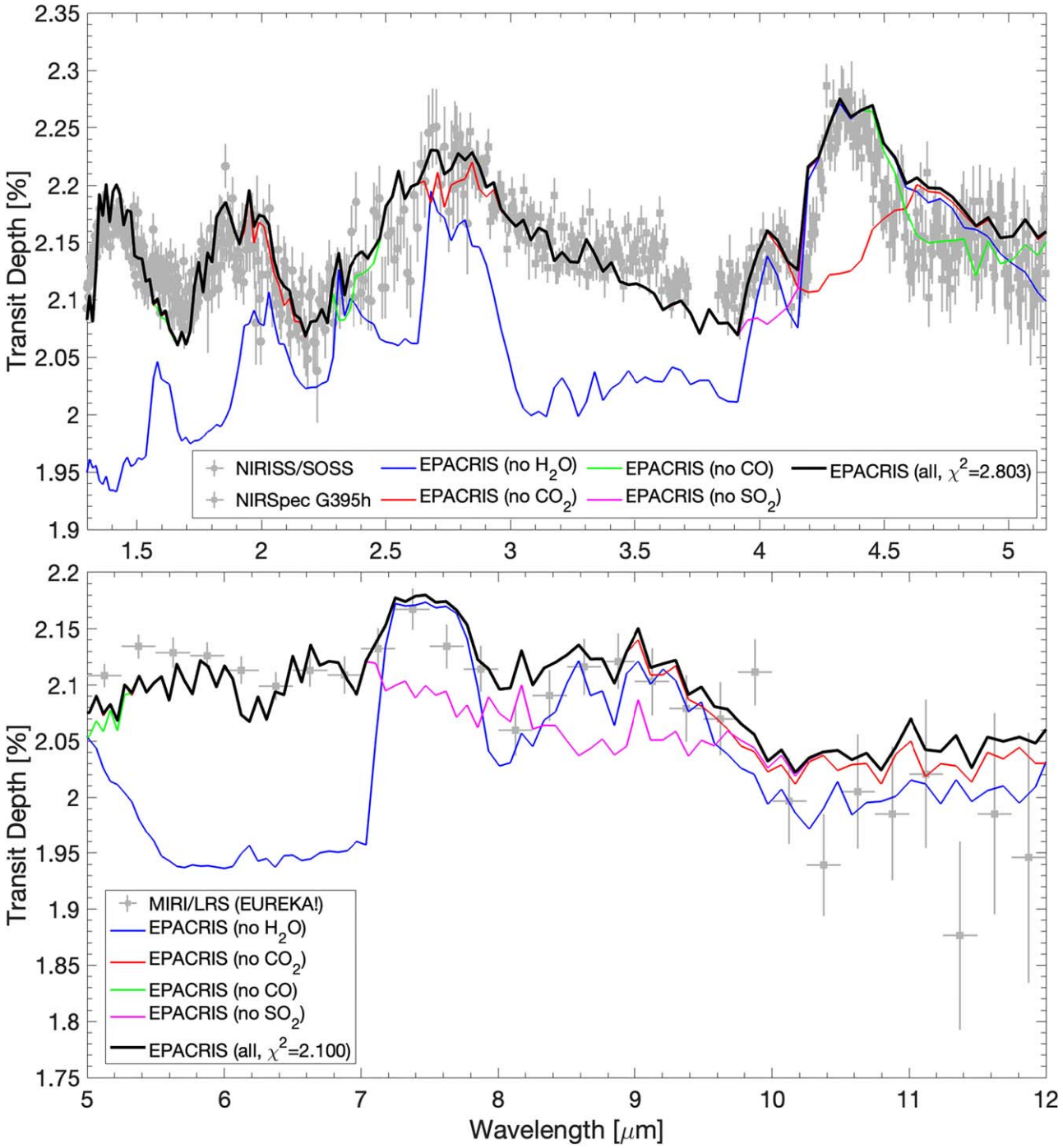

Figure 7. Comparison between the terminator-averaged theoretical transmission spectra generated by EPACRIS (solid lines) and the JWST observations. Top: NIRISS/SOSS and NIRSpec/G395H data (Alderson et al. 2023; Feinstein et al. 2023; the gray circle symbol points with error bars indicate NIRISS/SOSS data, while the gray square symbol points with uncertainties indicate NIRSpec G395h data). Bottom: MIRI/LRS data (Powell et al. 2024; the gray square symbol points with uncertainties). The uncertainties are 1σ standard deviations. The reduced χ^2 value for the near-infrared region was calculated against the NIRISS/SOSS and NIRSpec/G395H data, while the reduced χ^2 value for the mid-infrared region was calculated against the MIRI/LRS data. Each color represents a spectrum generated by excluding specific species: blue for no H_2O, red for no CO_2, green for no CO, magenta for no SO_2, and black for all species included.

CO_2 and SO_2. Additionally, the spectral feature near 3 μm could signify the presence of NH_3 or HCN, both anticipated to exceed 1 ppm at pressures below 1 mbar (Figure 8). This observation underscores the need for more detailed exploration in this wavelength range, potentially through repeated observations. Overall, similar to the WASP-39 b case, there is a decent agreement between the model predictions and the observational data for the WASP-80b atmosphere.

3.3. Future Applications and Limitations of the Current Study

The current framework—automatic reaction mechanism generation coupled with 1D photochemical kinetic-transport modeling—has numerous potential applications for tools used in studying (exo)planetary atmospheres. One application is in the realm of climate modeling. Accounting for disequilibrium chemistry is essential in climate modeling. Consequently, reducing the size of the photochemical network becomes

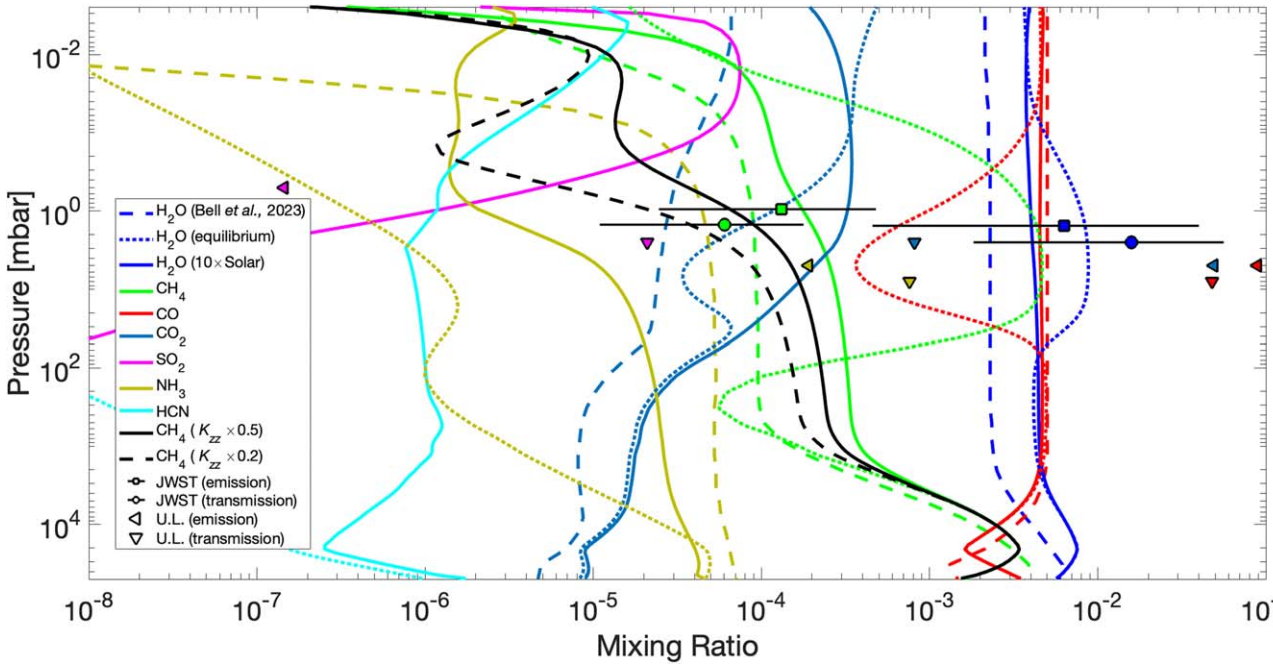

Figure 8. Comparison of the vertical molecular mixing ratio profiles for WASP-80 b's atmosphere: previous JWST observations (Bell et al. 2023; symbols and dashed lines) vs. current EPACRIS simulations (solid lines for 1D photochemical kinetic-transport modeling; dotted lines for thermochemical equilibrium). The square symbols with uncertainties indicate the emission data, and the circle symbols with uncertainties indicate the transmission spectra. The left-pointing triangle symbols indicate the upper-limit (U.L.) values determined from emission spectra, while the downward-pointing triangle symbols indicate the upper-limit values determined from transmission spectra. Each color indicates the corresponding species (SO_2: magenta; H_2O: blue; CH_4: green; CO: red; CO_2: dark blue; NH_3: yellow; and HCN: cyan). The dark solid and dashed lines are the predicted CH_4 volume mixing ratios when using a two times slower K_{zz} profile and a five times slower K_{zz} profile in Figure 3(b), respectively. Although not shown, the H_2O volume mixing ratio using a two times slower K_{zz} profile is almost identical to the H_2O volume mixing ratio using the original K_{zz} profile of WASP-80 b.

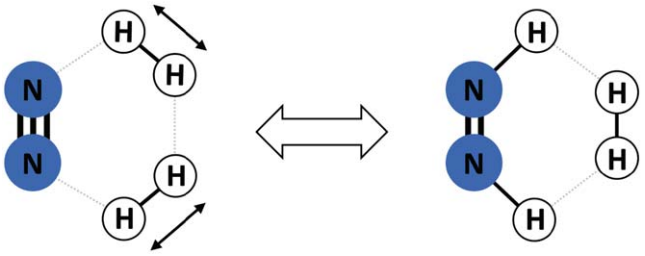

Figure 9. A schematic diagram that visualizes the first reaction (N_2+H_2+H_2→N_2H_2+H_2) in Scheme (28). From the left side, N_2 reacts with two H_2 molecules to form *cis*-N_2H_2 and H_2 on the right side.

crucial, especially since 2D or 3D climate modeling is computationally intensive. This challenge is amplified in the context of general circulation modeling (GCM).

To address this, it is important to retain major chemical species that significantly impact climate structure, while pruning less significant species from the chemical network to enhance computational efficiency. The current framework can offer substantial benefits to climate modeling and GCMs by eliminating unimportant species and reactions. Pruning can be achieved by adjusting features in the RMG, such as increasing the user-specified error tolerance, ϵ, or limiting the total number of atoms. However, this process involves a trade-off between minimizing the network size and maintaining the precision of the chemical network, necessitating a balance between these two aspects.

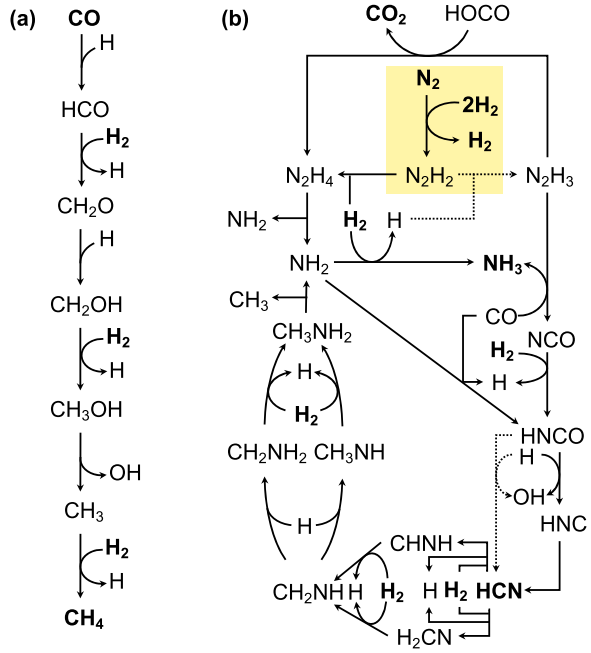

Figure 10. Model-predicted major reaction pathways at the deep interior ($P \sim 3\times10^4$ mbar) for (a) CO–CH_4 conversion, and (b) N_2–NH_3–HCN conversion. The bold characters represent major species with a mixing ratio above 1 ppm. The dashed pathways indicate directions at least three times slower than other branching reactions (e.g., N_2H_2 branching into N2H3 is three times slower than into N_2H_4). The yellow highlighted region in (b) indicates a newly suggested initial nitrogen incorporation path in the RMG-generated chemical network.

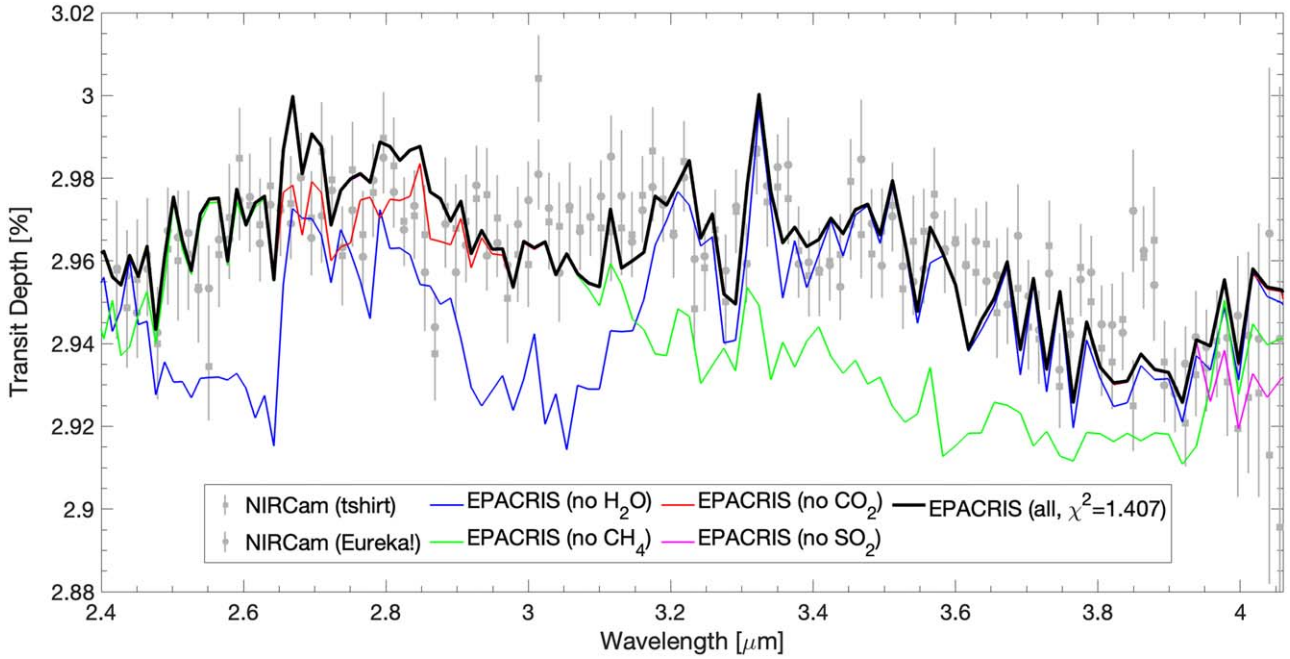

Figure 11. Comparison between the theoretical transmission spectra generated by EPACRIS (solid lines) and JWST observations: NIRCam tshirt (gray square symbol points with uncertainties) and Eureka! (gray circle symbol points with uncertainties) reductions by Bell et al. (2023). The uncertainties are 1σ standard deviations. The reduced χ^2 value of 1.407 was calculated against the NIRCam tshirt reduction data. Although not shown, the reduced χ^2 value against the NIRCam Eureka! reduction data was 1.748. Each color represents a spectrum generated by excluding specific species: blue for no H_2O, red for no CO_2, green for no CH_4, magenta for no SO_2, and black for all species included.

Moreover, several areas within the current framework could be improved. For instance, since RMG was primarily developed for simulating combustion chemistry, it lacks photochemical reactions in its library and does not account for vertical mixing processes (e.g., molecular diffusion and eddy diffusion). This omission might lead to significant gaps in identifying atmospherically important chemical species and reactions involving photons and vertical mixing. Therefore, incorporating photochemistry and physical processes in reaction mechanism generation is a critical area for future study.

4. Conclusions

In this study, we have developed a new framework for exoplanet atmospheric photochemical modeling. This framework, for the first time, integrates a rate-based automatic chemical network generator (RMG) with a 1D photochemical kinetic-transport atmospheric simulator, forming the chemistry module of EPACRIS. We first constructed a reaction network specifically tailored for the atmosphere of H_2-dominated hot Jupiters whose equilibrium temperatures are 800–1500 K, and then incorporated this chemical network into EPACRIS for 1D photochemical kinetic-transport modeling. Our model results generally align with previous studies of WASP-39 b by Tsai et al. (2023), particularly in capturing the photochemical production of OH radicals from H_2O photolysis in the upper atmosphere and the formation of SO_2 through successive oxidation by OH and H radicals. A key difference between our study and previous models is the predicted SO_2 abundance in the middle atmosphere (pressure range of 0.5–10 mbar). Our results indicate higher SO_2 formation at the warmer evening terminator compared to the cooler morning terminator. This discrepancy is attributed to the increased presence of sulfur species oxidizers (OH and H radicals), predominantly generated from thermally driven reactions between sulfur-bearing species (such as S or S_2) and H_2O within this middle atmosphere. The predicted transmission spectrum of the atmosphere of WASP-39 b based on our model was compared to the JWST NIRISS/SOSS, NIRSpec/G395H, and MIRI/LRS observations (Alderson et al. 2023; Feinstein et al. 2023; Powell et al. 2024), showing good consistency and capturing H_2O, CO_2, and SO_2 spectral features for a $10\times$ solar metallicity atmosphere. Our model result for WASP-80 b shows that deep-interior chemistry and vertical mixing dominate the general atmospheric chemistry, with predicted concentrations of CH_4, H_2O, CO, NH_3, HCN, and SO_2 exceeding 1 ppm at pressures below 1 mbar. Utilizing RMG, we identified a dominant, previously overlooked reaction for the initial nitrogen incorporation ($N_2+2\ H_2\rightarrow N_2H_2+H_2$), significant in high-pressure environments like deep-interior atmospheres. Such use of RMG can unveil new reactions within chemical networks, potentially leading to the discovery of novel species in (exo)planetary atmospheres. The predicted transmission spectrum of the atmosphere of WASP-80 b based on our model was compared to the JWST NIRCam observations reported by Bell et al. (2023), showing good consistency and capturing H_2O and CH_4 spectral features. This new approach not only provides the 1D photochemical kinetic-transport modeling of (exo)planetary atmospheres with unprecedented efficiency and preciseness, but also with applicability to diverse atmospheric conditions (e.g., from H_2-dominated to H_2O-dominated atmospheres), enabling us to more effectively and precisely predict and interpret the vast amounts of data from upcoming JWST observations of various exoplanet atmospheric conditions.

Acknowledgments

The authors thank Shang-min Tsai, Julianne Moses, Sean Jordan, and Diana Powell for discussions on the choice of

reaction rate coefficients involving H_2S thermal dissociation. The authors thank Taylor Bell for providing the WASP-80 b observation data and Diana Powell for providing the WASP-39 b observational data. This research work was carried out at the Jet Propulsion Laboratory, California Institute of Technology, under a contract with the National Aeronautics and Space Administration. This research work was funded by the Caltech-JPL President's and Director's Research and Development Fund. © 2024. California Institute of Technology. Government sponsorship acknowledged.

Software: EPACRIS (Hu et al. 2012, 2013; Hu & Seager 2014; Hu 2019), RMG (Gao et al. 2016; Liu et al. 2021; Johnson et al. 2022; Developers of RMG 2024).

Appendix
Thermochemical Equilibrium in the Atmosphere of WASP-39b

Figure A1 presents a comparison between the thermochemical equilibrium and photochemical steady-state vertical molecular mixing ratios of major species. These profiles were both simulated in the current study using EPACRIS.

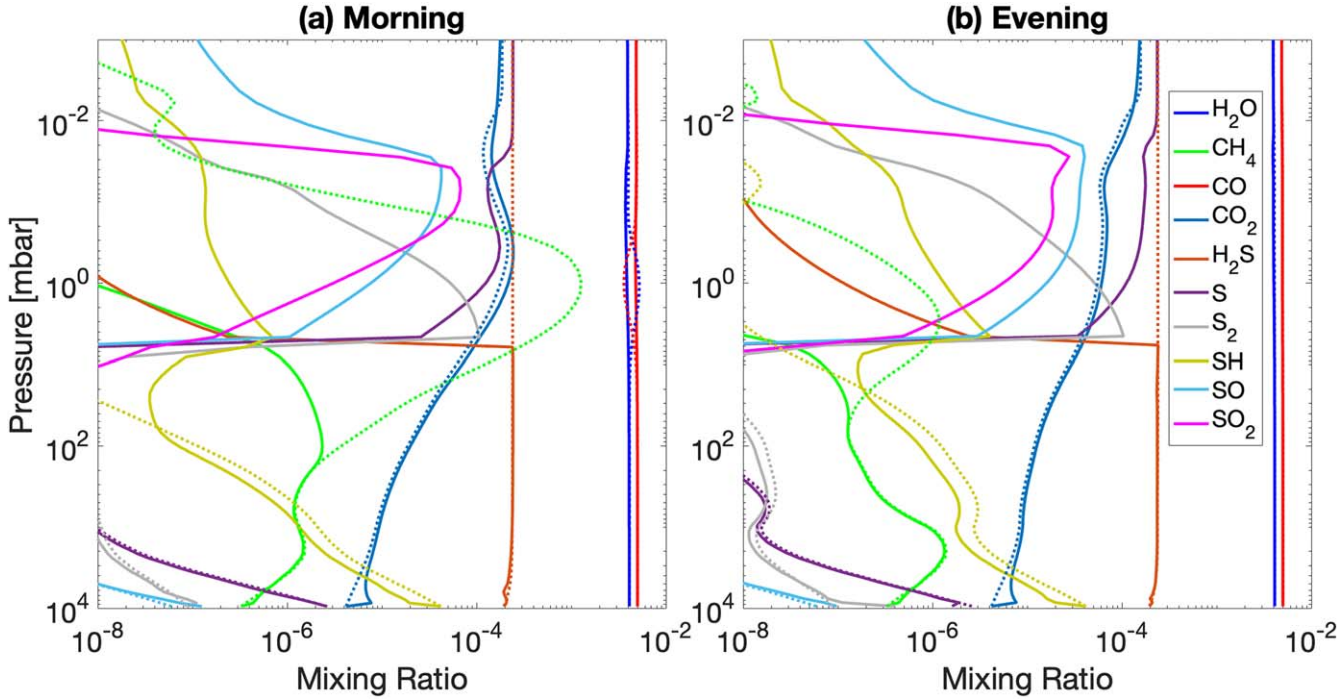

Figure A1. Comparison between the thermochemical equilibrium vertical molecular mixing ratio profiles of major species simulated for the (a) morning and (b) evening terminators (dashed lines) and photochemical steady-state vertical molecular mixing ratio profiles of major species simulated from the current work using EPACRIS (solid lines). Each color indicates the corresponding species (SO_2: magenta; H_2O: blue; CH_4: green; CO: red; CO_2: dark blue; H_2S: brown; S: purple; S_2: gray; SH: yellow; and SO: light blue).

ORCID iDs

Jeehyun Yang https://orcid.org/0000-0002-1551-2610
Renyu Hu https://orcid.org/0000-0003-2215-8485

References

Ahrer, E.-M., Stevenson, K. B., Mansfield, M., et al. 2023, Natur, 614, 653
Alderson, L., Wakeford, H. R., Alam, M. K., et al. 2023, Natur, 614, 664
Asatryan, R., Bozzelli, J. W., Silva, G. D., Swinnen, S., & Nguyen, M. T. 2010, JPCA, 114, 6235
Bell, T. J., Welbanks, L., Schlawin, E., et al. 2023, Natur, 623, 709
Benson, S. W., & Buss, J. H. 2004, J. Chem. Phys., 29, 546
Chase, M. W. J., & Buss, J. H. 1985, J. Phys. Chem. Ref. Data, 14, https://cir.nii.ac.jp/crid/1570291225512139136
Chu, T.-C., Buras, Z. J., Oßwald, P., et al. 2019, PCCP, 21, 813
Class, C., Liu, M., Vandeputte, A. G., & Green, W. H. 2016, PCCP, 18, 21651
Dana, A. G., Buesser, B., Merchant, S. S., & Green, W. H. 2018, Int. J. Chem. Kinet., 50, 243
Developers of RMG, 2024 Reaction Mechanism Generator (RMG) version 3.2.0, GitHub, https://github.com/ReactionMechanismGenerator
Dong, X., Pio, G., Arafin, F., et al. 2023, JPCA, 127, 3231
Faedi, F., Barros, S. C., Anderson, D. R., et al. 2011, A&A, 531, A40
Feinstein, A. D., Radica, M., Welbanks, L., et al. 2023, Natur, 614, 670
Fleury, B., Gudipati, M. S., Henderson, B., & Swain, M. 2019, ApJ, 871, 158
Fleury, B., Gudipati, M. S., Henderson, B., & Swain, M. 2020, ApJ, 899, 147
Gao, C. W., Allen, J. W., Green, W. H., & West, R. H. 2016, CoPhC, 203, 212
Goodwin, D. G., Speth, R. L., Moffat, H. K., & Weber, B. W., 2021 Cantera: An Object-oriented Software Toolkit for Chemical Kinetics, Thermodynamics, and Transport Processes, Zenodo
Goos, E., Burcat, A., & Ruscic, B. 2016, Extended Third Millennium Thermodynamic Database of New NASA Polynomials with Active Thermochemical Tables update, Institute of Chemistry, Eötvös University (ELTE), https://garfield.chem.elte.hu/Burcat/NEWNASA.TXT
Hu, R. 2019, ApJ, 887, 166
Hu, R. 2021, ApJ, 921, 27
Hu, R., Damiano, M., Scheucher, M., et al. 2021, ApJL, 921, L8
Hu, R., & Seager, S. 2014, ApJ, 784, 63
Hu, R., Seager, S., & Bains, W. 2012, ApJ, 761, 166
Hu, R., Seager, S., & Bains, W. 2013, ApJ, 769, 6
Hwang, D.-Y., & Mebel, A. M. 2003, JPCA, 107, 2865
Johnson, M. S., Dong, X., Grinberg Dana, A., et al. 2022, J. Chem. Inf. Model., 62, 4906
Johnson, M. S., Nimlos, M. R., Ninnemann, E., et al. 2021, Int. J. Chem. Kinet., 53, 915
JWST Early Release Science Team, Ahrer, E.-M., Alderson, L., et al. 2023, Natur, 614, 649
Keçeli, M., Elliott, S. N., Li, Y.-P., et al. 2019, PComI, 37, 363
Liu, M., Chu, T.-C., Jocher, A., et al. 2020, Int. J. Chem. Kinet., 53, 27
Liu, M., Grinberg Dana, A., Johnson, M. S., et al. 2021, J. Chem. Inf. Model., 61, 2686
Lodders, K. 2020, Solar Elemental Abundances (Oxford: Oxford Univ. Press),
Loyd, R. O. P., France, K., Youngblood, A., et al. 2016, ApJ, 824, 102
Madhusudhan, N., Piette, A. A. A., & Constantinou, S. 2021, ApJ, 918, 1
Madhusudhan, N., Sarkar, S., Constantinou, S., et al. 2023, ApJL, 956, L13
McBride, B. J., & Gordon, S. 1992, Computer Program for Calculating and Fitting Thermodynamic Functions (Washington, DC: NASA)
McBride, B. J., Zehe, M. J., & Gordon, S. 2002, NASA Glenn Coefficients for Calculating Thermodynamic Properties of Individual Species (Washington, DC: NASA), https://ntrs.nasa.gov/citations/20020085330
Moses, J. I., Marley, M. S., Zahnle, K., et al. 2016, ApJ, 829, 66
Moses, J. I., Visscher, C., Fortney, J. J., et al. 2011, ApJ, 737, 15
Norinaga, K., Janardhanan, V. M., & Deutschmann, O. 2008, Int. J. Chem. Kinet., 40, 199
Powell, D., Feinstein, A. D., Lee, E. K., et al. 2024, Natur, 626, 979
Rimmer, P. B., & Rugheimer, S. 2019, Icar, 329, 124
Rustamkulov, Z., Sing, D. K., Mukherjee, S., et al. 2023, Natur, 614, 659
Sarathy, S. M., Vranckx, S., Yasunaga, K., et al. 2012, CoFl, 159, 2028
Schwer, D. A., Tolsma, J. E., Green, W. H., & Barton, P. I. 2002, CoFl, 128, 270
Shiell, R. C., Hu, X. K., Hu, Q. J., & Hepburn, J. W. 2000, JPCA, 104, 4339
Song, Y., Hashemi, H., Christensen, J. M., et al. 2017, Int. J. Chem. Kinet., 49, 37
Triaud, A. H., Gillon, M., Ehrenreich, D., et al. 2015, MNRAS, 450, 2279
Tsai, S.-M., Lee, E. K. H., Powell, D., et al. 2023, Natur, 617, 483
Tsai, S.-M., Lyons, J. R., Grosheintz, L., et al. 2017, ApJS, 228, 20
Tsai, S.-M., Malik, M., Kitzmann, D., et al. 2021, ApJ, 923, 264
Vandewiele, N. M., Van Geem, K. M., Reyniers, M.-F., & Marin, G. B. 2012, ChEnJ, 207-208, 526
Veillet, R., Venot, O., Sirjean, B., et al. 2024, A&A, 682, A52
Venot, O., Hébrard, E., Agundez, M., et al. 2012, A&A, 546, A43
Wogan, N. F., Batalha, N. E., Zahnle, K., et al. 2024, ApJL, 963, L7
Yang, J., Gudipati, M. S., Henderson, B. L., & Fleury, B. 2023, ApJ, 947, 26
Yu, X., Moses, J. I., Fortney, J. J., & Zhang, X. 2021, ApJ, 914, 38
Yung, Y. L., Allen, M., & Pinto, J. P. 1984, ApJS, 55, 465